

# Probing Right-Handed Neutrinos at Current and Future Colliders through Displaced Lepton Jets

A Thesis

submitted to

Indian Institute of Science Education and Research Pune  
in partial fulfillment of the requirements for the  
BS-MS Dual Degree Programme

by

Divya Gadkari

Reg. No. 20121062



Indian Institute of Science Education and Research Pune  
Dr. Homi Bhabha Road,  
Pashan, Pune 411008, INDIA.

April, 2017

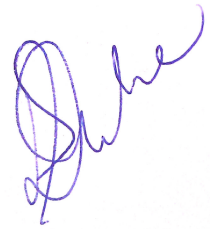
Supervisor: Dr. Sourabh Dube

© Divya Gadkari 2017

All rights reserved

# Certificate

This is to certify that this dissertation entitled Probing Right-Handed Neutrinos at Current and Future Colliders through Displaced Lepton Jets towards the partial fulfilment of the BS-MS dual degree programme at the Indian Institute of Science Education and Research, Pune represents study/work carried out by Divya Gadkari under the supervision of Dr. Sourabh Dube, Assistant Professor, Department of Physics, during the academic year 2016-2017.



Dr. Sourabh Dube



Divya Gadkari

Committee:

Dr. Sourabh Dube

Dr. Arun Thalapillil



This thesis is dedicated to my mother, Prajakta Gadkari.

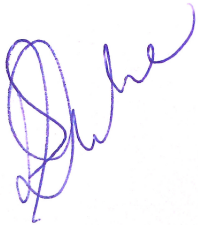


# Declaration

I hereby declare that the matter embodied in the report entitled Probing Right-Handed Neutrinos at Current and Future Colliders through Displaced Lepton Jets are the results of the work carried out by me at the Department of Physics, Indian Institute of Science Education and Research, under the supervision of Dr. Sourabh Dube and the same has not been submitted elsewhere for any other degree.



Divya Gadkari



Dr. Sourabh Dube





# Acknowledgments

I would like to express my deepest gratitude to Prof. Sourabh Dube, for his constant guidance over the past 3 years. It was his continued encouragement and support that kept me motivated to work hard. I am also very grateful to Prof. Arun Thalapillil for his extremely valuable inputs and helpful discussions which helped the project to progress.

I want to thank Prof. Seema Sharma and the whole of IISER EHEP group for providing useful suggestions throughout this thesis. Special thanks to Shubhanshu Chauhan for the continuous supply of new ideas and stimulating discussions, and helping me with everything, starting from generating background samples to providing company for coffee breaks!

Thanks to my mom, dad and sister for their relentless support and encouragement. Last but not the least, thanks to all my friends and the physics room gang for making life a little more interesting!



# Abstract

In this thesis, the sensitivity of searches for the  $\nu$ MSM model in a 13 TeV and a 100 TeV hadron-hadron collider, were compared. The  $\nu$ MSM predicts heavy right-handed neutrinos which mix with the SM neutrinos. This model was studied for the signal phase space of  $M_N \lesssim 16$  GeV, for a multileptonic final state. All the final decays were forced to muons, to get a signal topology of a prompt muon + a leptonic jet, comprised of muons lying close to each other. Backgrounds were estimated for this final state. The sensitivity reach of a 13 TeV collider for this signal phase space was found for a luminosity of  $30 \text{ fb}^{-1}$  and  $300 \text{ fb}^{-1}$ . The sensitivity reach of a 100 TeV hadron collider for this signal phase space was found for a luminosity of  $300 \text{ fb}^{-1}$  and  $3 \text{ ab}^{-1}$ . It was found to improve for the  $\sqrt{s}=100$  TeV hadron-hadron collider as compared to the 13 TeV collider for  $300 \text{ fb}^{-1}$  of luminosity. It was observed to further improve for the 100 TeV hadron-hadron collider for  $3 \text{ ab}^{-1}$  of luminosity.



# Contents

<b>Abstract</b>	<b>xi</b>
<b>1 Introduction</b>	<b>7</b>
1.1 Problems of the Standard Model . . . . .	8
<b>2 The sub-weak right-handed neutrino model</b>	<b>11</b>
2.1 Type-I See-Saw . . . . .	11
2.2 The RHN model . . . . .	12
2.3 Previous Studies . . . . .	14
<b>3 Signal and background simulation</b>	<b>17</b>
3.1 Signal simulation . . . . .	19
3.2 Background simulation . . . . .	20
<b>4 Detecting muons at the CMS experiment</b>	<b>23</b>
<b>5 Analysis Strategy</b>	<b>27</b>
5.1 Search for low mass RHN . . . . .	27
<b>6 RHN studies at the LHC</b>	<b>31</b>
6.1 Cross checking with data . . . . .	31

6.2	Sensitivity study at 13 TeV . . . . .	38
<b>7</b>	<b>RHN studies at a 100 TeV hadron collider</b>	<b>43</b>
7.1	Signal selection . . . . .	44
7.2	Result . . . . .	46
<b>8</b>	<b>Conclusion</b>	<b>47</b>
<b>9</b>	<b>Appendix</b>	<b>51</b>

# List of Tables

3.1	Signals for 13 TeV using FullSim . . . . .	19
3.2	Backgrounds for 13 TeV using FullSim . . . . .	21
3.3	Backgrounds for 13 TeV and 100 TeV . . . . .	21
6.1	Number of events passing the pre-selection and selection for signal, background and data for $5.89 \text{ fb}^{-1}$ of data . . . . .	37
6.2	Number of events passing selection for the sensitivity study, in signal points BP1 and BP2 and background, of luminosity $30 \text{ fb}^{-1}$ . . . . .	40
7.1	Number of events passing selection for the sensitivity study, in signal points BP1 and BP2 and background, of luminosity $300 \text{ fb}^{-1}$ . . . . .	46
8.1	Signal acceptance for 13 TeV and 100 TeV . . . . .	49
9.1	Details about background samples generated using CMS FullSim at 13 TeV . . . . .	51
9.2	Signal cross-sections for 13 TeV and 100 TeV using DELPHES . . . . .	52





# List of Figures

1.1	Standard Model particles [6] . . . . .	8
2.1	Feynman diagram depicting the production of the RHN via $W^\pm$ boson decay. The $W^\pm$ decays into the RHN and a prompt muon ( $W^\pm \rightarrow \mu^\pm N$ ) and the RHN can decay into a muon and a $W^\pm$ boson decaying to muon and muon neutrino ( $N \rightarrow \mu^\pm W^\mp \rightarrow \mu^\pm \mu^\mp \nu_\mu$ ) (left) a muon neutrino and a Z boson decaying to a pair of muons ( $N \rightarrow Z \nu_\mu \rightarrow \mu^\pm \mu^\mp \nu_\mu$ ) (right) . The final state comes out to be one $\mu^\pm$ + system of $(\mu^\pm \mu^\mp \nu_\mu)$ . . . . .	13
2.2	On the left is the separation between the muons of the MuonJet for three different RHN masses of $M_N = 2$ GeV ,8 GeV and 16 GeV . On the right, is the distance from the primary vertex in XY plane, for the MuonJet muons for three different values of the mixing parameter, $ V_\mu ^2 = 2 \times 10^{-3}, 10^{-4}, 10^{-6}$ , $M_N = 2$ GeV mass point . . . . .	14
2.3	The cross section in picobarns for $\sqrt{s}=13$ TeV (left) and 100 TeV (right) in the mass-mixing plane. Also shown are the black dots depicting the signal points generated and used for interpolation. . . . .	15
4.1	A cross sectional view of the CMS detector. Muons leave a signal in the silicon tracker, as well as the Muon chambers. [67] . . . . .	24
5.1	The $p_T$ of the prompt muon (left), the $p_T$ of the MuonJet muons (right). . .	28
5.2	The transverse impact parameter, $ d_{xy} $ of the prompt muon (left), and the MuonJet muons (right). . . . .	29
5.3	The $\Delta R$ between the prompt muon and the MuonJet (left), and the minimum $\Delta R$ between any pair of muons (right). . . . .	29

6.1	The invariant mass distribution for a two prompt muon selection. The agreement between data and background shows the successful application of the trigger efficiency and muon identification and reconstruction scale factors. . . .	32
6.2	The $p_T$ of the prompt muon (a), the $\Delta R$ between the prompt muon and MuonJet (b), the invariant mass of the MuonJet (c), and the relative track isolation of MuonJet (d). . . . .	35
6.3	(a) $p_T$ of the prompt muon with $M(\mu_1, \mu_2, \mu_P) < 40$ GeV (left) and the missing transverse energy when $M(\mu_1, \mu_2, \mu_P) > 80$ GeV (right) . . . . .	35
6.4	The $M(\mu_1, \mu_2, \mu_P)$ (a), and the $\Delta\phi$ between the prompt muon and the leading muon from the MuonJet (b). The invariant mass distribution shows contributions due to asymmetric conversions at the $Z$ -mass. . . . .	36
6.5	The $\Delta R$ between the prompt muon and the MuonJet (left) and the invariant mass of the MuonJet shown between 0 and 10 GeV (right). . . . .	37
6.6	$\Delta R$ between $\mu_1$ and $\mu_2$ from MuonJet after vetoing a second prompt . . . . .	38
6.7	Acceptance for signal selections described in Section 6.1 (left) and acceptance for selections described in Section 6.2 (right) for a 13 TeV collider . . . . .	40
6.8	Exclusion contour at 13 TeV for integrated luminosity of $30 \text{ fb}^{-1}$ (left) and $300 \text{ fb}^{-1}$ (right). Each figure shows the contours for signal efficiency of 100%, 70%, and 50%. In each case, the selection is assumed to be 100% efficient for SM background. . . . .	41
7.1	Various kinematic properties for the final state are compared at 13 TeV, and 100 TeV. The $\eta$ of MuonJet muons (top, left), the eta of the prompt muon (top, right), the momentum ( $ \vec{p} $ ) of MuonJet muons (middle, left), the $ \vec{p} $ of the prompt muon (middle, right), the $p_T$ of MuonJet muons (bottom, left), and the $p_T$ of the prompt muon (bottom, right). Aside from the $\eta$ , all other distributions do not show large difference. . . . .	45
7.2	Exclusion contour at 100 TeV for integrated luminosity of $300 \text{ fb}^{-1}$ (left) and $3 \text{ ab}^{-1}$ (right). Each figure shows the contours for signal efficiency of 100%, 70%, and 50%. In each case, the selection is assumed to be 100% efficient for SM background. . . . .	46

8.1 Exclusion contours at  $\sqrt{s} = 13$  TeV and 100 TeV for signal efficiency of 100%. For the same luminosity of  $300 \text{ fb}^{-1}$ , the 100 TeV collider has a higher reach than the 13 TeV one. This is due to increase in signal acceptance and cross-section at the 100 TeV collider. The reach of the 100 TeV collider further increases, corresponding to a luminosity of  $3 \text{ ab}^{-1}$  of data. . . . . 48



# Chapter 1

## Introduction

The standard model of particle physics (SM) describes all the currently known particles and the interactions between them. It is based on a quantum field theory, which has been remarkably successful in explaining all precision measurements over time. The framework of the SM gives an understanding of strong, weak and electromagnetic interactions, and has successfully incorporated all the known particles in it. The Higgs boson, thought to be the last missing piece of the SM and was discovered by the CMS and ATLAS experiment in 2012. [1] - [2]. A comprehensive review of all the experimental measurements of SM particles can be found in [3].

In the SM, the fundamental interactions of the strong and EW forces are mediated by spin-1 bosons, where as matter is made up by spin 1/2 fermions. The electromagnetic force is mediated via photons,  $\gamma$ , the weak force via three bosons, the  $W^\pm$  and  $Z$  and the strong force via eight gluons, all represented by  $g$ . The fermions are divided into two categories : leptons and quarks. There are in total, 12 leptons and 36 quarks, where only the quarks can interact via the strong force. The spontaneous symmetry breaking of the electroweak theory, imparts mass to the  $W$  and  $Z$  gauge bosons. The Higgs mechanism predicts the existence of a scalar (spin 0) Higgs boson. The particles in the SM acquire mass through interactions with the Higgs field. [4]-[5] Fig. 1.1 depicts a standard way of showing the fermions (in 3 generations) and the gauge bosons and Higgs.

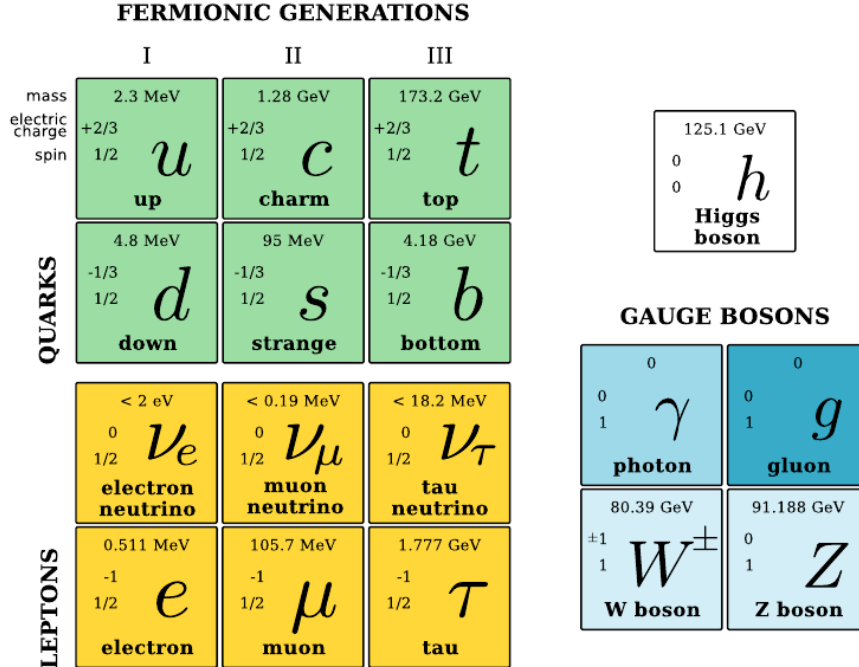


Figure 1.1: Standard Model particles [6]

## 1.1 Problems of the Standard Model

Even though the standard model has been a widely successful theory, there are some issues which it fails to address. This section will briefly list down the inadequacies of the SM, and go into the detail of neutrino masses, which the SM fails to explain. [6] - [8]

The SM does not include the gravitational force, one of the fundamental forces of nature. Though gravity is negligible at the current collider energies, it would become comparable with the other forces at the Planck scale ( $\sim 10^{19}$  GeV).

The universe has an imbalance between baryonic and antibaryonic matter. It is predominantly made up of baryonic matter. The standard model cannot explain this asymmetry.

The galaxy rotation curves cannot be explained by the distribution of visible matter in the universe and suggest the existence of dark matter [9]. Dark matter is named so as it does not as it does not appear to interact electromagnetically or via other forces, but only gravitationally. [10]. Explanation of dark matter could come from the perspective of particle

physics and in that case, SM fails to provide any dark matter candidate.

The ultraviolet cutoff of the SM,  $\Lambda_{UV}$ , is assumed to be at the Planck scale  $\sim 10^{19}$  GeV. The Higgs mass acquires radiative corrections which are quadratically dependent on  $\Lambda_{UV}$ , but as measured by CMS and ATLAS [1] - [2], the actual Higgs mass is of the order of magnitude of  $\sim 10^2$  GeV. This implies a very fine-tuning in cancellation of the quantum correction terms, which is considered unnatural. This is known as the hierarchy problem and SM does not give any explanation for this conundrum.

The SM also fails to explain why there is a mass hierarchy between the three generations of fermions. The first generation of fermions are much lighter than the third generation. For example the mass of the up quark is 2.3 MeV while the mass of the top quark is about 172.4 GeV. This order of magnitude difference between the masses of different generations has not been accounted for by the SM.

### 1.1.1 Unsolved question of neutrino masses

Another puzzle which the SM fails to solve is that of neutrino masses. The SM neutrinos are leptons which exist in three flavors (  $e, \tau, \mu$  ) and interact via the weak force. They are not charged under electromagnetic force, or the strong force. Thus they do not interact electromagnetically or via the strong force. The experiment done by C. S. Wu *et al* in 1957 showed that parity was violated and that the neutrinos are always of the left-handed helicity, that is, their spin and direction of motion always points in the opposite direction [11]. The SM predicted neutrinos to be massless which would mean they would travel at the speed of light in vacuum,  $c$ . Given that the massless neutrinos travel at  $c$ , their helicity is Lorentz-invariant.

In 1968 the Homestake experiment, which aimed to measure solar electron neutrinos, indicated the flux of the neutrinos were much lower than the theoretical prediction [12]. Over the years, additional data taking as well as other experiments observed the electron neutrino flux to be half of the predicted values [13], [14]. These observations were bolstered by the solar neutrino flux measurements in Sudbury Neutrino Observatory (SNO) [15] and the atmospheric neutrino flux measurements at the Super-Kamiokande experiment [16]. These observations are successfully explained by the phenomenon of neutrino oscillations, that is,

the oscillations between the flavors of a neutrino.

Neutrino oscillations are a consequence of the flavor eigenstates of neutrinos being different from the mass eigenstates of neutrinos. The flavor eigenstate can be written as a superposition of the mass eigenstates and vice versa . Equation 1.1 shows the relation between the mass and flavor eigenstate of neutrinos, where  $U$  is a lepton flavor mixing matrix or the Pontecorvo-Maki-Nakagawa-Sakata (PMNS) [17] - [21] matrix. [22]

$$|\nu_\alpha\rangle = \sum_{k=1}^3 U_{\alpha k} |\nu_k\rangle \quad (1.1)$$

The probability of a neutrino of flavour  $\alpha$  oscillating into a flavor of  $\beta$  is dependent on  $\sin\left(\frac{\Delta m_{kj}^2 L}{4E}\right)$ , where  $\Delta m_{kj}^2 = m_k^2 - m_j^2$  and  $m_k, m_j$  are all possible pairs of mass eigenstate. The neutrino starts off with the flavor  $\alpha$  and is detected with the flavor  $\beta$  after travelling a distance  $L$ , with an energy  $E$ . Hence, if all the neutrinos are massless (or of the same mass), neutrino oscillation would not take place. Therefore, the discovery of neutrino oscillation indicate that atleast one of the SM neutrino has to be massive [14].

A puzzle which still needs to be solved is the very small masses of neutrinos. The discovery of neutrino oscillations gave evidence for SM neutrino masses, but the reason for very small masses of the SM neutrino is still unsolved. There are many theories beyond standard model (BSM), which try to address all the above mentioned issues. The  $\nu$ MSM model is one such model, and Chapter 2 will describe it in detail.



# Chapter 2

## The sub-weak right-handed neutrino model

As described in Chapter 1, the SM is insufficient to explain all the phenomena in nature and the sub-weak RHN model tries to resolve all these problems. This model, known as the neutrino minimal SM ( $\nu$ MSM) [23] - [25] and referred throughout this document as the RHN model introduces three Right-handed sterile neutrinos (RHN). Though there are other models which predict an RHN of any possible mass, the  $\nu$ MSM assumes them to be below the electro-weak scale. The RHN model uses Type-I see-saw mechanism [26] to explain the low masses of SM neutrinos, and the next section will briefly describe this mechanism, after which the RHN model will be described in detail.

### 2.1 Type-I See-Saw

This section will describe Type-I seesaw mechanism, used by the RHN model. A very general lagrangian for electroweak interactions contains two types of neutrino mass terms, the Dirac and Majorana mass terms. The Dirac mass terms is of the form

$$\mathcal{L}_D \sim -m_D(\bar{\nu}_L\nu_R + \bar{\nu}_R\nu_L) \quad (2.1)$$

while the majorana mass term is of the form

$$\mathcal{L}_M \sim -\frac{1}{2}m_M^L(\bar{\nu}_L\nu_L^c + \bar{\nu}_L^c\nu_L) - \frac{1}{2}m_M^R(\bar{\nu}_R\nu_R^c + \bar{\nu}_R^c\nu_R) \quad (2.2)$$

When we write these in matrix form we get the following expression

$$\mathcal{L}_{general} = -\frac{1}{2}(\bar{\nu}_L\bar{\nu}_R^c)\mathcal{M}\begin{pmatrix} \nu_L \\ \nu_R^c \end{pmatrix} \quad (2.3)$$

where

$$\mathcal{M} = \begin{pmatrix} m_M^L & m_D \\ m_D & m_M^R \end{pmatrix} \quad (2.4)$$

Here  $\nu_L$  and  $\nu_R$  are the flavor eigenstates of the neutrinos. When we diagonalise the matrix  $\mathcal{M}$ , we would obtain the mass eigenvalues and mass eigenstates of the neutrinos. To explain the very low masses of the SM neutrinos, the matrix  $\mathcal{M}$  is assumed to be such that  $m_M^R \approx 0$ ,  $m_M^L \approx M_P \approx 10^{14} - 10^{16}$  GeV and  $m_D \approx m_{fermion}$ , that is  $m_D$  is the order of charged lepton or quark masses. When we diagonalize this matrix, we get the eigenvalues  $M_1 \sim M_P$  and  $M_2 \sim m_{fermion}^2/M_P$ . Since one of the mass eigenvalues come out to be very large while the other is a very small value, this is known as the seesaw mechanism [27]- [30]. The RHN model uses this mechanism and solves the issue of the small masses of neutrinos through the introduction of the heavy right-handed neutrino of relatively heavy masses. The following section will describe the model in a little more detail.

## 2.2 The RHN model

As given earlier the RHN model predicts the existence of three sterile right-handed neutrinos. The mass of these neutrinos ( $M_N$ ) and the mixing of these neutrinos ( $|V_\alpha|$ ) with the SM neutrino of flavor  $\alpha$ , are the free parameters of the model. The interactions of these RHN are completely determined by the mixing parameter  $|V_\alpha|$ . Hence, all their coupling constants with SM particles, will be the coupling constants of the SM neutrinos multiplied by a factor

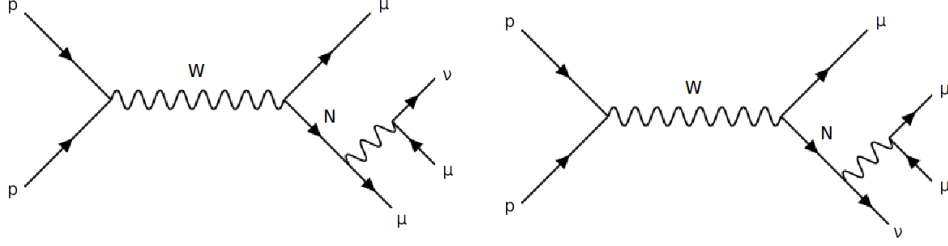


Figure 2.1: Feynman diagram depicting the production of the RHN via  $W^\pm$  boson decay. The  $W^\pm$  decays into the RHN and a prompt muon ( $W^\pm \rightarrow \mu^\pm N$ ) and the RHN can decay into a muon and a  $W^\pm$  boson decaying to muon and muon neutrino ( $N \rightarrow \mu^\pm W^\mp \rightarrow \mu^\pm \mu^\mp \nu_\mu$ ) (left) a muon neutrino and a Z boson decaying to a pair of muons ( $N \rightarrow Z \nu_\mu \rightarrow \mu^\pm \mu^\mp \nu_\mu$ ) (right) . The final state comes out to be one  $\mu^\pm +$  system of  $(\mu^\pm \mu^\mp \nu_\mu)$

$|V_\alpha|$  [31].

For our analysis, we consider a simplified version of this model. The search is carried out for only one flavor of the RHN, which is assumed to mix only with the muon neutrino of the standard model. This is motivated by the clean signatures obtained by taking muons in the final state, as explained further in this section. This is done by setting  $|V_e|^2 = 0 = |V_\tau|^2$ . Thus the free parameters of the theory are now the mass of the RHN, and  $|V_\mu|^2$  . Fig. 2.1 shows the Feynman diagrams of the decay channel through which the RHN is probed, to give three muons and a SM muon neutrino in the final state. Thus in this study, the final state gives a multi-lepton signature [31].

As the mass of the RHN decreases, it becomes boosted. The RHN is produced through the decay of an on-shell  $W$  boson. Due to this, as the mass of the RHN decreases, its boost increases. Thus the angular distance between the decay products of the RHN decreases. Shown in Fig. 2.2 (a), is the angular distance between the two daughter muons of RHN for three values of  $M_N$  : 2 GeV , 8 GeV and 16 GeV RHN. As the mixing angle between the RHN and SM neutrino decreases, its lifetime increases. This is because a lower mixing angle implies lower coupling of the RHN with SM particles. A long-lived RHN, after being produced at the primary vertex, would travel some distance before decaying into muons. Hence its two muon daughters and the muon neutrino are produced at a displaced vertex. [31] Shown below in Fig. 2.2 (b) is the transverse impact parameter ( $|d_{xy}|$ ) of a 2 GeV RHN for the different mixing angles of  $|V_\mu|^2 = 2 \times 10^{-3}, 10^{-4}, 10^{-6}$ .

In this study, we choose a topology that is sensitive primarily to RHN with mass  $\lesssim 16$

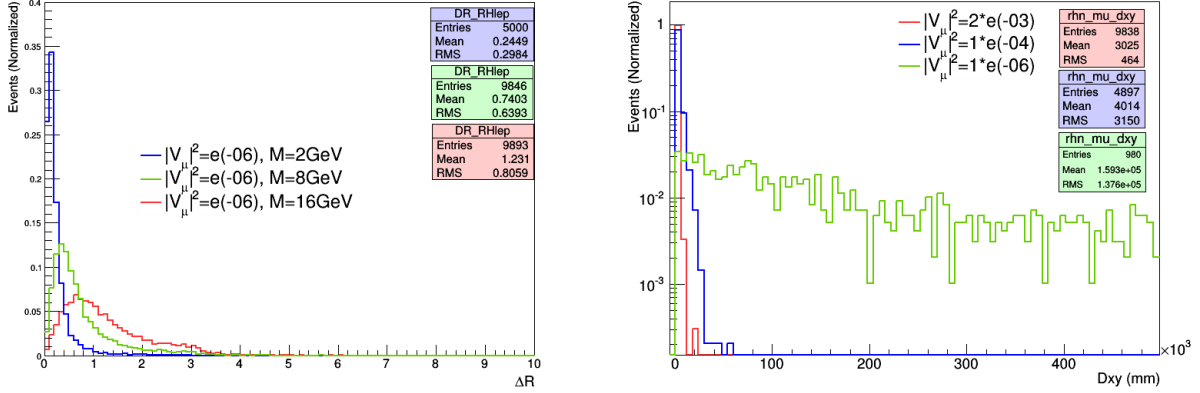


Figure 2.2: On the left is the separation between the muons of the MuonJet for three different RHN masses of  $M_N = 2 \text{ GeV}$ ,  $8 \text{ GeV}$  and  $16 \text{ GeV}$ . On the right, is the distance from the primary vertex in XY plane, for the MuonJet muons for three different values of the mixing parameter,  $|V_\mu|^2 = 2 \times 10^{-3}$ ,  $10^{-4}$ ,  $10^{-6}$ ,  $M_N = 2 \text{ GeV}$  mass point

GeV. At these masses, the signal consists of a prompt muon coming from the decay of W and a pair of muons coming from the RHN, which lie very close to each other. This pair of muons will be referred to as, a system of MuonJet, throughout this study. At lower values of  $|V_\mu|^2$ , the MuonJet system can be displaced from the primary vertex. Hence, the final signature consists of a prompt muon + a MuonJet system. Using muons has an advantage over using electrons, as muon signatures are cleaner. Fig. 2.3 shows the production cross-section of the RHN in the mass-mixing plane for a  $\sqrt{s} = 13 \text{ TeV}$  and  $100 \text{ TeV}$  hadron-hadron collider.

## 2.3 Previous Studies

Different phase spaces of mass and mixing of the RHN model have been probed by various experiments [27], [32]-[45]. RHN of masses below  $0.5 \text{ GeV}$  have been excluded for mixing above  $|V_\mu|^2 = 10^{-10}$ . Most of the RHN's between masses of  $0.5 \text{ GeV}$  to  $2 \text{ GeV}$  have been excluded for a mixing above  $|V_\mu|^2 = 10^{-7}$  or more. For the phase space of masses above  $2 \text{ GeV}$ , most of the RHN of mixing above  $|V_\mu|^2 = 10^{-5}$  have been excluded. CMS and ATLAS have probed the signal phase space of  $M_N > 40 \text{ GeV}$  and have excluded RHN for a mixing above  $|V_\mu|^2 = 10^{-5}$  or more [45]-[49]. Signal region of  $M_N < 15 \text{ GeV}$  are not yet probed by these experiments, and in this study we explore the sensitivity of collider experiments to this scenario. Additionally, searches for models giving LeptonJets in the final state have

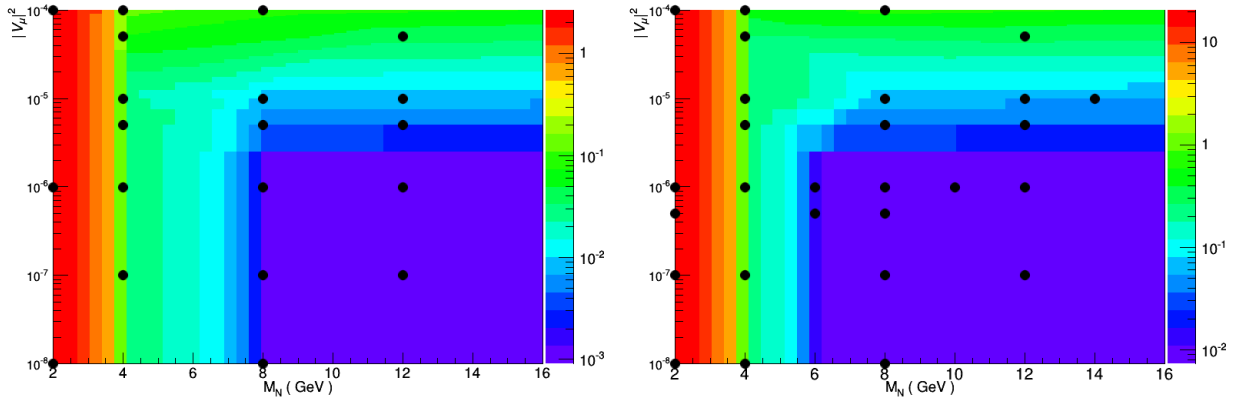


Figure 2.3: The cross section in picobarns for  $\sqrt{s}=13$  TeV (left) and 100 TeV (right) in the mass-mixing plane. Also shown are the black dots depicting the signal points generated and used for interpolation.

been done previously [55]-[50], though the topology explored in these searches are not the same as the one in this thesis.



# Chapter 3

## Signal and background simulation

A collision event can be generated and simulated by standard software using Monte Carlo techniques. There exist several generators to produce output for standard model processes. These generators may differ in ways such as the precision of calculation, the choice of fragmentation and hadronization models, and so on. MADGRAPH [58] is a next-to-leading order (NLO) generator for standard model, and BSM processes. PYTHIA [56] - [57] is a LO generator, which can also perform parton showering and hadronization unlike Madgraph. Both of these can generate BSM processes. The typical method is to start with a FEYNRULES [59] output file. The FEYNRULES package contains the information on the Lagrangian of a QFT model, giving all the couplings constants, branching ratios and Feynman rules in the model-file, in a format which can be taken as an input for any MC generators.

The softwares that are used to generate the collisions are colloquially termed as MC generators. These MC generators can simulate processes occurring in a hadron-hadron collider and calculate their cross-sections. The cross-sections depend on all the coupling constants and branching ratios of the model and the Parton Distribution Functions (pdf's) [60]. The coupling constants come from the input model-file from FEYNRULES and specific PDFs can be chosen to be used in the generation process using LHAPDF [61]. MADGRAPH is an MC event generator which generates events and calculates the cross-section upto next-to-leading order (NLO). Through MADGRAPH one has the freedom to generate specific processes in a given framework of a model, with specific PDF's and kinematic cuts on the particles being generated, along with being able to change the centre-of-mass energy of the two colliding

protons. Through the MADGRAPH software, one can input the parameters of the theory and can impose kinematic selections.

The second step in an event simulation is the parton showering and hadronization. Just like charged particles radiate photons, colored particles radiate gluons and additionally, these colored gluons can also radiate further gluons. This creates a parton shower, which can be modeled using different event generators. In nature, only color-neutral particles exist, and thus colored objects hadronize to give us colorless hadrons and jet clustering algorithms are optimized to identify hadrons coming from a single hadron. PYTHIA8 is an event generator which has been used throughout this study, for parton shower and hadronization of output of madgraph. Though PYTHIA8 can be used as MC event generator as well, in this study it has been used for only for hadronizing the output of MADGRAPH MC events .

The third step involves passing the hadronized MC event through a detector simulation. When all the generated particles from a particular event pass through the detector, they pass through the matter of the detector and interact with it to give us 'hits'. These signals can be generated due to various interactions. Electrons travel through the detector and can lose their energy via processes such as bremsstrahlung, while other charged particles can deposit their energy in the detector via coulombic interactions causing ionization or excitation of atoms of the detector matter. Photons can interact in the matter causing photoelectric effect, Compton scattering or pair-production depending on their energy. A hadron can interact with the nuclei in the detector via strong interactions, to deposit their energy [62]. In a real detector, we are blind to the real processes which take place in a p-p collision, but instead 'reconstruct' an event to get all the processes using all the hits in the detector. A simulation of the detector does not only simulate the detector geometry but also emulates the reconstruction algorithms used in the real particle physics experiments, where CMS is one such detector. The official simulation of the CMS detector, CMSSW uses the GEANT4 [63]-[64] toolkit to simulate the passage of particles through the detector elements. DELPHES [65] is a program that aims to emulate the effects of detector simulation. It does this by parametrizing the response of a multipurpose detector to physics objects such as electrons, photons, muons, charged and neutral hadrons. The full simulation of CMS is used for cross-checking our study using data, while DELPHES is used for sensitivity study of the RHN model at 13 TeV and 100 TeV collider. The following sections describe the signal and background samples generated using the three steps, in detail.



## 3.1 Signal simulation

### 3.1.1 Signal simulation for validation in FullSim for 13 TeV

For the validation of the 13 TeV studies using data, two signal samples were generated using MADGRAPH v5. The hadronization and parton showering were simulated using PYTHIA v8 and the hadronized output was then passed through the full simulation (FullSim) of the CMS detector based on GEANT 4. Once this is done, the simulated signal is reconstructed with the same algorithm used for reconstructing real data at the CMS. Two benchmark points (BP) were produced with the CMS full simulation, which are : *BP1*:  $M_N = 2$  GeV,  $|V_\mu|^2 = 10^{-4}$  and *BP2*:  $M_N = 4$  GeV,  $|V_\mu|^2 = 10^{-5}$  . Table 3.1 depicts the cross-sections and the luminosities of the signal produced.

Benchmark Point	Mass ( $M_N$ )	Mixing ( $ V_\mu ^2$ )	$\sigma$ (pb)	Luminosity ( $\text{fb}^{-1}$ )
<i>BP1</i>	2 GeV	$10^{-4}$	2.9019	16.937
<i>BP2</i>	4 GeV	$10^{-5}$	0.0221	2067.87

Table 3.1: Signals for 13 TeV using FullSim

### 3.1.2 Signal simulation for sensitivity study at 13 TeV and 100 TeV

The time taken for generating an event using full simulation is of the order  $\sim 100$ s, while the time taken for generating an event in a parametric simulation such as DELPHES is of the order  $\sim 10$ ms. Since generating samples using the full simulation takes a lot of time, especially for the displaced objects like the N, sensitivity studies were done by generating samples using DELPHES . To get the sensitivity of our selections, signal points of different mass and mixing were generated using MADGRAPH v5, hadronized by PYTHIA v8 and passed through DELPHES for both 13 TeV and 100 TeV studies. The efficiency and resolution of a detector, in detecting and measuring a particle's momentum and energy, depends upon the kind of particle which passes through it, the kinematics of the particle, as well as its spatial position in the detector. All the information about this detector response is stored in detector cards. Sensitivity studies for the 13 TeV were done using the CMS card, 'delphes\_card.CMS.tcl'

and 100 TeV collider were done using the FCC-hh card, ‘delphes\_card\_FCC.tcl’ in DELPHES . Since the detector for such a 100 TeV collider has not been constructed yet, its efficiency of reconstruction and retaining the information of truth objects is yet unknown. Hence using generated level objects instead of reconstructed level objects proves to be advantageous as these studies can be extrapolated to data like objects by simply applying different detector efficiencies. Table 9.2 in the appendix lists down the signal points generated and their respective cross-section. As shown the cross-section of the signal points goes up approximately by a factor of 7 in a 100 TeV collider as compared to a 13 TeV one.

## 3.2 Background simulation

### 3.2.1 Background simulation for validation in FullSim for 13 TeV

Samples to estimate the background at 13 TeV were produced using FullSim. For hadronization PYTHIA 8 has been used and all the samples were passed through the Full simulation of CMS and reconstructed using the same algorithm which is used for actual data at the CMS. Table 3.2 summarises the cross-section and the luminosities of the MC backgrounds. All the samples used were officially produced by CMS and Table 9.1 in the Appendix contains the details of these CMS samples . In addition to these, backgrounds such as different resonances like  $J/\psi$  which is not accounted by  $W$ +jets could also contribute in the signal region. Rare backgrounds, that is backgrounds with low productional cross-section, such as WZ and ZZ decaying into muons can contribute in the signal region. The background of hadronic jets, known as QCD background, could fake muons and be a potential background. All these backgrounds would need to be estimated using rigorous methods and data driven techniques, and have not been included in this study. All of the backgrounds, generated for cross-checking our study using data, have been listed in Table 3.2 along with the generators used to produce them.

Background	$\sigma(pb)$	Luminosity ( $fb^{-1}$ )	Generator
$W$ +jets	61526.7	0.4585	MADGRAPH +PYTHIA
$DY$ +jets	5765	8.6511	MADGRAPH +PYTHIA
$t\bar{t}$ -semiLep	114	83.0638	MADGRAPH +PYTHIA
Single Top t-channel+jets	44.33	297.619	AMCatnlo+PYTHIA
Single Top s-channel+jets	3.36	73.9725	POWHEG+PYTHIA

Table 3.2: Backgrounds for 13 TeV using FullSim

### 3.2.2 Background simulation for sensitivity study at 13 TeV and 100 TeV

The primary backgrounds arise from semileptonic top-pair production ( $t\bar{t}$ -semiLep) and production of heavy flavor jets in association with a  $W$  boson ( $Wcc$ ).  $t\bar{t}$ -semiLep refers to the background where both of the top quarks decay to a  $W$  and a  $b$ -quark. One of the  $W$  decays leptonically, while the  $W$  can decay hadronically or leptonically ( $t\bar{t} \rightarrow W^+W^+b\bar{b} \rightarrow \ell^+\nu qq\bar{b}$ ). The  $Wcc$  background refers to the associated production of a  $W$  boson with  $c\bar{c}$ -quarks.  $t\bar{t}$ -semiLep is the dominating background for both 100 TeV and 13 TeV scenarios. It is expected that background from hadronic jets, termed as the QCD background, and the single top background, might also start contributing in the 100 TeV collider as compared to the 13 TeV collider as the cross-section of all processes, especially processes involving strong processes, goes up by orders of magnitude as shown in Table 3.3. These backgrounds will be further elaborated in Sec. 6.1.2.

Background	$\sigma$ (pb) (13 TeV)	$\sigma$ (pb)(100 TeV)
$W(\rightarrow \nu l)+cc$	14.9	191.02
$t\bar{t}(\rightarrow \nu lbb + jets)$	141	7852

Table 3.3: Backgrounds for 13 TeV and 100 TeV



# Chapter 4

## Detecting muons at the CMS experiment

The CMS detector was built to probe for a wide range of new physics, and is operational at proton-proton center-of-mass energy of  $\sqrt{s}= 13$  TeV in 2017. The CMS detector consists of a 3.8 T superconducting solenoid. Inside volume of the solenoid lie the hadronic calorimeter (HCal) made up of alternating layers of brass and scintillator, the electromagnetic calorimeter (ECal) made up of lead-tungstate crystals, the silicon strip tracker and finally closest to the beam line, the silicon pixel tracker. Outside the solenoid, the steel return yoke is embedded with the muon chambers. All of these detector components consists of a module in the barrel along with a module in the end-cap region [66]. All charged objects give a track in the silicon tracker, while neutral particle like a photon pass through without interacting with it. In the ECal, electron and photons deposit all their energy, while in the HCal all hadronic jets deposit their energy. Muons give a track in the inner tracker, do not deposit all their energy in the calorimeters and pass through to give a track in the outer muon chamber. Fig 4.1 shows a cross-sectional view of the CMS detector, along with how different particles interact with it.

Since the amount of data generated at the LHC is huge and cannot all be stored, it is collected via online triggers. These triggers store only relevant events for a study and use online reconstruction. Thus, before an event is stored it has to fire a trigger, which come in two stages. The first stage is the Level 1 (L1) trigger, and the second stage is the High

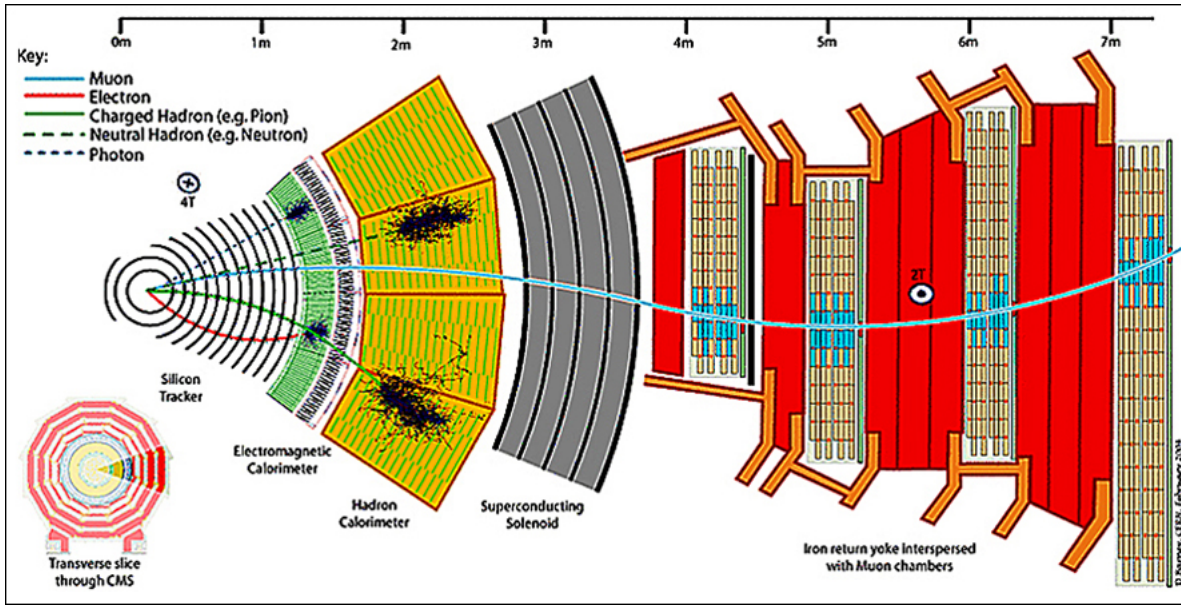


Figure 4.1: A cross sectional view of the CMS detector. Muons leave a signal in the silicon tracker, as well as the Muon chambers. [67]

Level Trigger (HLT). The event first has to pass the L1 trigger where the decision to keep it or not is made in orders of micro-second. Next the event has to pass the HLT, where an improved online reconstruction is done to decide whether to pass the event. Once the event passes these two stages it is stored for further analysis. For this study, the final state consists of muons. Hence, the signal events could pass triggers which require atleast one muon with some quality conditions imposed on it. A muon can be detected at two different places in the detector, the inner tracker, where all charged objects give a track, and the outer muon chambers, which are gas ionization. Unlike electrons which deposit all their energy in the ECal, or hadrons which deposit all their energy in the HCal muons interact minimally with the calorimeters, and hence can be detected in the outer muon chambers. can give a signal in two separate subdetectors. It can be used to reconstruct the track of the muon as it travelled through the detector, while the bending of the track can be used to find the momentum of the muon. In the barrel region ( $|\eta| < 2.0$ ), the momentum resolution is about 1% for a 100 GeV muon. For reconstructing a track of a muon, hits in the outer muon system are taken as input and matched to form a stand-alone muon. Similarly, a track is reconstructed by fitting the hits in the inner tracker. The tracks in the outer muon chamber are then matched with the tracks compatible inner track, to form a global muon track. In scenarios where objects are long-lived and decay only after travelling a certain distance from the main interaction

point, the muons resulting after the decay from such objects have a high chance of being Standalone muons. In this study, we would expect to get global as well as standalone muons, depending on the lifetime of the RHN. The following chapter describes an analysis strategy which can be used to probe this model, using muons in the final state.





# Chapter 5

## Analysis Strategy

In this chapter a general strategy is designed to probe for the RHN model. The RHN can be produced via a W boson, which decays into the RHN and a lepton (  $e, \mu, \tau$  ), where the probability of production of different leptons depends on the mixing of the RHN to the SM neutrinos.

We design a search optimized for the RHN which mixes only with the muon SM neutrino, and is forced to decay to only muons. We specifically probe for the signal phase space of  $M_N \lesssim 16$  GeV, and the following section describes the search strategy used to probe for this signal.

### 5.1 Search for low mass RHN

As given in Chapter 2, for the signal phase space of  $M_N < 15$  GeV, the RHN is boosted, and as the mixing decreases it also starts to have longer lifetime [31]. Thus, the decay of the RHN results in a pair of muons which lie very close to each other and are displaced from the primary interaction point. Hence, the final signature we need to probe consists of one prompt muon, coming from the W boson, and a pair of displaced muons lying very close to each other, coming from the RHN. In this study the signal phase space of  $M_N \lesssim 16$  GeV is probed. The sensitivity of this search is expected to go down for higher masses, due to the imposition of  $\Delta R$  cut. This search will be elaborated in the following few lines.

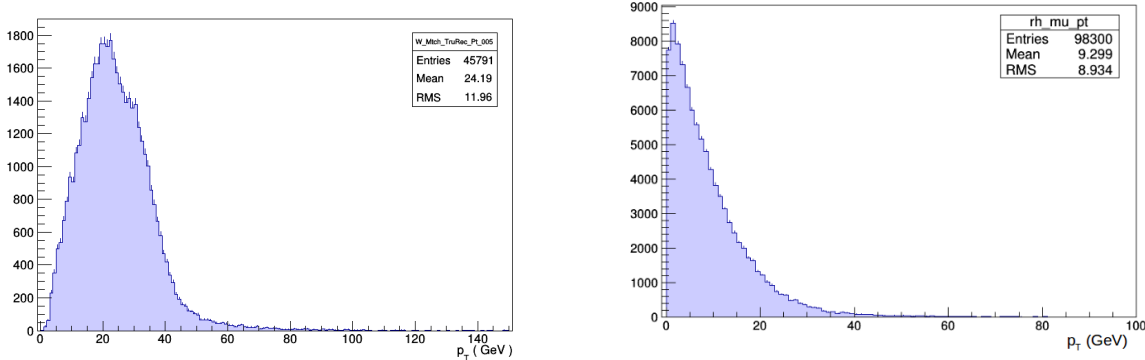
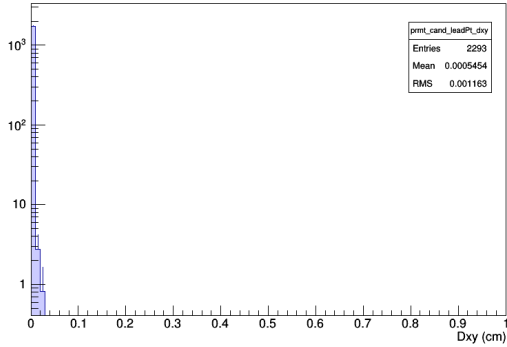


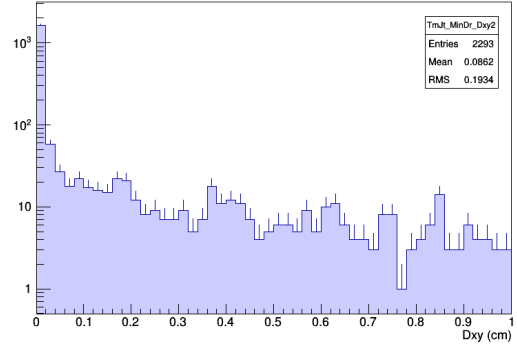
Figure 5.1: The  $p_T$  of the prompt muon (left), the  $p_T$  of the MuonJet muons (right).

For the online selection of a signal event, the event should contain a triggerable object. The prompt muon can satisfy the isolation and  $p_T$  requirements of a trigger. Fig 5.1 depicts the  $p_T$  of the prompt for the signal point BP1. Fig 5.3 depicts the  $\Delta R$  between the prompt muon and the MuonJet system, which shows that they are back-to-back, indicating that the prompt muon is isolated. In addition to these the muon has to have  $p_T > 22$  GeV, based on the threshold of the current triggers at CMS. Additionally, a cut on  $|\eta|$  of the muons is imposed. Since the prompt muons is isolated, a cut on relative isolation of the prompt, defined as  $\frac{\sum p_T^{TRK}}{p_T^\mu}$  is imposed. Here  $p_T^{TRK}$  refers to the  $p_T$  of any charged track and all the charged tracks within a cone of  $\Delta R = 0.4$  from the prompt muon and  $p_T^{TRK} > 1$  GeV are considered. Given that the muon is prompt, selections are made on the longitudinal and transverse impact parameters. The transverse impact parameter distribution for the prompt muon and the muons from the RHN are shown in Fig. 5.2.

For the pre-selection of MuonJet we cannot use the standard muon ID's since all the muon ID's require the muons to have atleast an inner track, which might not be the case for displaced MuonJet which have a track only in the outer muon chambers. Fig 5.1 depicts the  $p_T$  of the muons of a MuonJet system. For selection of the MuonJet pair, events where atleast one prompt exists are selected and in these events all possible pairs of muons with  $p_T > 2$  GeV and are formed, along with imposing cuts on their  $|\eta|$ . For example if we have three muons which satisfy the given  $p_T$  and  $|\eta|$  conditions, we would have three distinct pairs of muons, one muon paired with each of the remaining two. Amongst all these pairs, the pair with the minimum  $\Delta R$  is chosen. Fig 5.3 depicts the  $\Delta R$  between the muons of the pair having minimum  $\Delta R$ . The muons from this closest lying pair have to be opposite



(a)



(b)

Figure 5.2: The transverse impact parameter,  $|d_{xy}|$  of the prompt muon (left), and the MuonJet muons (right).

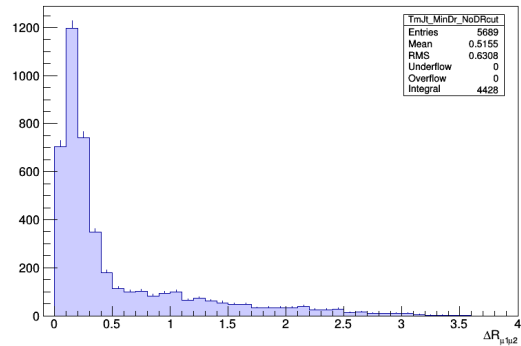
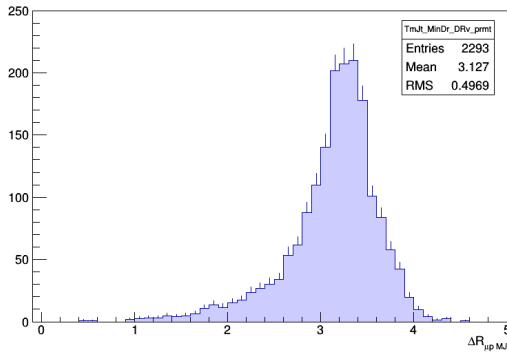


Figure 5.3: The  $\Delta R$  between the prompt muon and the MuonJet (left), and the minimum  $\Delta R$  between any pair of muons (right).

signed and in addition a cut of  $\Delta R_{MIN}$  is imposed since the muons from the RHN lie very close to each other. The two muons from the MuonJet have to be oppositely signed. Both of the two muons from the closest lying pair have to be simultaneously either global muons or standalone muons. When the RHN decays, both the muons will decay at the same point in the detector, and hence both of them are expected to give a track in the inner as well as outer tracker, or both of them are expected to give a standalone track in the outer chamber. It will be unlikely that one of the muons is a global muon while the other is a standalone, which might happen in the cases of inner and outer track mismatch, which would need much more rigorous studies.

Once the closest pair of muons satisfy all these conditions and the event has a third muon which is a prompt muon, we obtain a system of MuonJet in addition to a prompt muon. From hereon the two muons from MuonJet will be labelled as  $\mu_1$  and  $\mu_2$ , and the prompt muon will be labelled as  $\mu_P$ . After the preselection, final signal selection is made by imposing additional cuts to optimize the signal with respect to the backgrounds and the following chapters will describe these selections in detail, for the 13 TeV as well as 100 TeV collider scenario.

# Chapter 6

## RHN studies at the LHC

In this chapter, the RHN model is studied at a 13 TeV collider. For the RHN studies at the LHC, the signal selections and background estimation were cross-checked using data. Those studies were used to estimate the selections and backgrounds for the sensitivity study for both 13 and 100 TeV colliders. The following sections describe the studies of the RHN model at the 13 TeV collider.

### 6.1 Cross checking with data

This section describes the the cross-check of the background with data for the RHN model. Due to the unique signal topology and no previous studies at the LHC on a similar signature, it was necessary to unblind a small portion of the data to validate our background estimation. At the same time it is important to stay unbiased such that the signal selections are not affected by how the data looks. Hence all the MC backgrounds and signals were scaled to 5.89 fb<sup>-1</sup> of data, which makes up about 16% of the 13 TeV 2016 data. Here the HLT\_TkIsoMu22 (High Level Trigger) was used to collect data. It requires a muon with minimum  $p_T$  of 22 GeV at online reconstruction level. It also requires the muon to have a relative track isolation of  $\frac{\sum p_T^{TRK}}{p_T^\mu} < 0.40$ , where  $p_T^{TRK}$  is the  $p_T$  of any charged track at the detector. There is some efficiency associated with the trigger, due to which even if an event passes all the trigger criteria it might not pass through. The efficiency of HLT\_TkIsoMu22 with respect to  $p_T$  comes to about 85% in the plateau region which starts at 30 GeV . The MC acceptance has

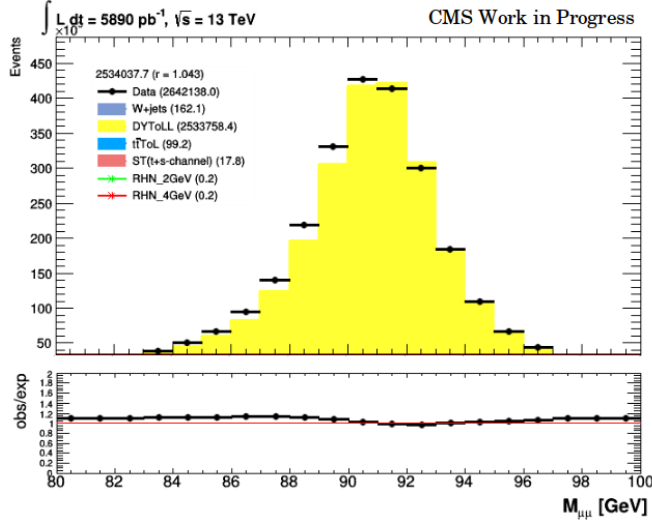


Figure 6.1: The invariant mass distribution for a two prompt muon selection. The agreement between data and background shows the successful application of the trigger efficiency and muon identification and reconstruction scale factors.

to be corrected to account for this trigger efficiency. This correction is done by scaling all the events of an MC with the efficiency factor. Note that this method is more efficient than simply selecting a fraction of events, corresponding to the trigger efficiency, in MC while rejecting other events. Even though rejecting the events would be emulating exactly what happens in data, scaling of all the events ensures that we do not lose out any statistics and retain all the information. Additionally, CMS prescribes some standard ID's for muons, and depending on the definition of a particular ID, muons can be loose, medium and tight ID. There are efficiencies associated with these ID's as well, for example a muon which passes all the requirements of the medium ID might still fail to pass the ID after being reconstructed. These ID efficiencies are not same for data and MC simulations, and the all the MC samples have been corrected for these ID scale factors.

To validate the application of trigger efficiency as well as the scale factors, we cross check the MC yield in a control region dominated by  $Z$  bosons. The control region is selected by requiring two muons of opposite charge with  $80 < M_{\mu\mu} < 100$  GeV and satisfying the condition  $\frac{\sum p_T^{TRK}}{p_T^\mu} < 0.25$ ,  $|d_{XY}| < 0.1\text{cm}$  and  $|d_Z| < 0.2\text{cm}$ . As seen in the Fig. 6.1 the DY MC sample agreed with the data within 5% and a scaling factor of 1.043 was applied to

it for all of the studies.

### 6.1.1 Event Pre-selection

The trigger requires a muon to be  $p_T > 22$  GeV with the Relative Isolation, defined as  $\frac{\sum p_T^{TRK}}{p_T^\mu} < 0.4$ , where all the charged tracks within a cone of 0.4 from the muon are considered. A cut of  $p_T > 22$  GeV will reject a lot of signal events ( 44% in 2 GeV signal points and 43.1% in the 4 GeV signal point ). Currently this is the lowest unrescaled single-muon trigger. All the other triggers are rescaled, using which, will decrease the event acceptance further. For the offline selection of the prompt muon, it is required to be a medium ID muon. Medium ID definition requires the muon to be global muon i.e. a muon which has a track in the tracker as well as the outer muon chamber. In addition to this it also has quality condition on global-tracks and how well the inner track matches with the standalone track in the outer muon chamber and all the quality cuts are standard values prescribed at CMS. In addition to this the muon has to have  $p_T > 22$  GeV ,  $|\eta| < 2.4$ . In addition to these, cuts on  $\frac{\sum p_T^{TRK}}{p_T^\mu} < 0.25$ , the transverse impact parameter  $|d_{XY}| < 0.1$  cm and impact parameter in the z direction,  $|d_Z| < 0.2$  cm are also imposed.

For the pre-selection of MuonJet, all possible pairs of muons in an event, with  $p_T > 2$ GeV and  $|\eta| < 2.4$  are considered. Once the pair of muons with the minimum  $\Delta R$  is chosen, a cut of  $\Delta R < 0.5$  is imposed. The two muons from the minimum  $\Delta R$  pair should be oppositely signed. The event should also have a third muon which satisfies all the prompt selection criteria. Thus, we obtain the two muons from the MuonJet  $\mu_1, \mu_2$ , and the prompt muon  $\mu_P$ .

### 6.1.2 Backgrounds

To have a robust study of the model it is of utmost importance to have a good background estimation. The non-standard topology of one prompt along with a pair of displaced MuonJet makes it challenging to estimate the background, as it involves non-isolated, soft muons which are displaced. Hadronic jets can give MuonJet like muons, and the MC simulations do not perfectly model this background. To do a rigorous study of the background, data driven techniques would need to be employed in addition to MC samples, to account for

fake background. Additionally, studies for such a topology have not been done before. It is seen that in fully reconstructed objects,  $W$ +jets is a major contributor of the background. The prompt muon can come from the  $W$ , whereas the jets can give us MuonJet like muons, through resonances such as  $J/\psi$  or  $b$ -quarks decaying into muons.  $DY$ +jets can also be a background, where the decay is forced to be leptonic. One of the leptons from the  $DY$  decay will give the prompt muon, while the other lepton can fake a MuonJet system, with a third muon coming from jets. Other backgrounds are  $t\bar{t}$  where atleast one of the top quarks has to decay leptonically while the other can decay hadronic or leptonically, and single top background in  $t$  and  $s$  channel. The available  $W$ +jet sample was statistically limited and corresponded to a small integrated luminosity. [ Section 3.2.1 ] Due to this the scale factor was very high, leading to high uncertainties in the signal region. Section 3.1.1 and 3.2.1 describe all the backgrounds and signal MC samples generated.

Fig. 6.2 shows the stacked plots of all the estimated backgrounds. Signal points BP1, BP2 and the data have been overlaid with the stacked plots of background, where BP2 is scaled ten times its contribution. The estimated background with the preselection accounts for the observed data to within 20%. This assures us that the considered sources of background are adequate to carry our further sensitivity issues. Two regions which were used to test the background estimation were  $M(\mu_1, \mu_2, \mu_P) < 40$  GeV and  $M(\mu_1, \mu_2, \mu_P) > 80$  GeV , where  $M(\mu_1, \mu_2, \mu_P)$  is the invariant mass of  $\mu_1, \mu_2$ , and  $\mu_P$ , as given in Fig. 6.3. In the first figure the  $p_T$  of the prompt has been depicted for the control region of  $M(\mu_1, \mu_2, \mu_P) < 40$  GeV . Here the total integral of data and background agree within 83%. The second figure depicts the missing transverse energy for the control region  $M(\mu_1, \mu_2, \mu_P) > 80$  GeV . In this control region the data and the background agree within 85%.

### 6.1.3 Event Selection

Additional requirements beyond preselection are made to further increase sensitivity to signal.  $\mu_1$  and  $\mu_2$  are required to have  $|d_{XY}| > 1$  mm. A cut on the invariant mass of the three muons is imposed such that events with  $80 \text{ GeV} < M(\mu_1, \mu_2, \mu_P) < 100 \text{ GeV}$  are vetoed. This is to cut down on  $DY$  contribution. Asymmetric conversion refers to the process where a  $Z$  boson decays into a pair of muons, where one of the muons radiates a photon, which further pair produces into two muons whose energy is distributed asymmetrically. Due to the asymmetric distribution of the energy between the muons coming from the photon conversion,



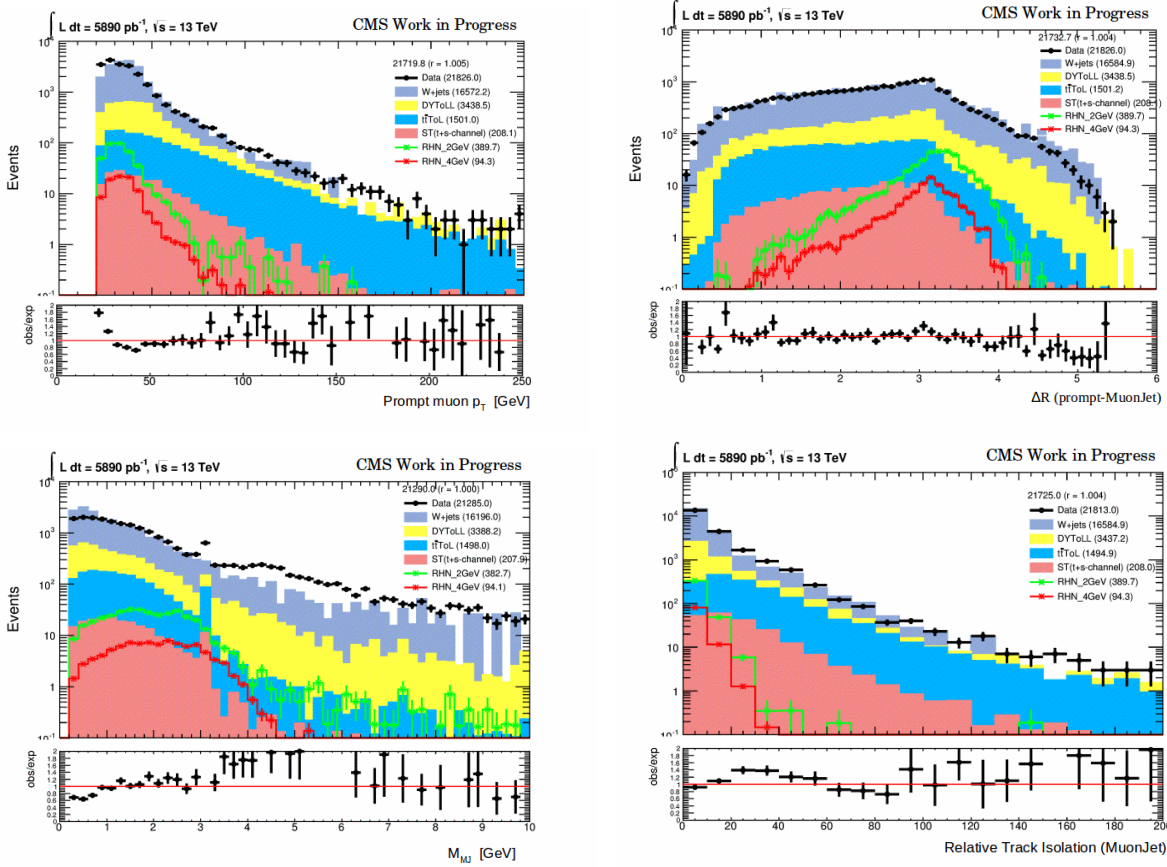


Figure 6.2: The  $p_T$  of the prompt muon (a), the  $\Delta R$  between the prompt muon and MuonJet (b), the invariant mass of the MuonJet (c), and the relative track isolation of MuonJet (d).

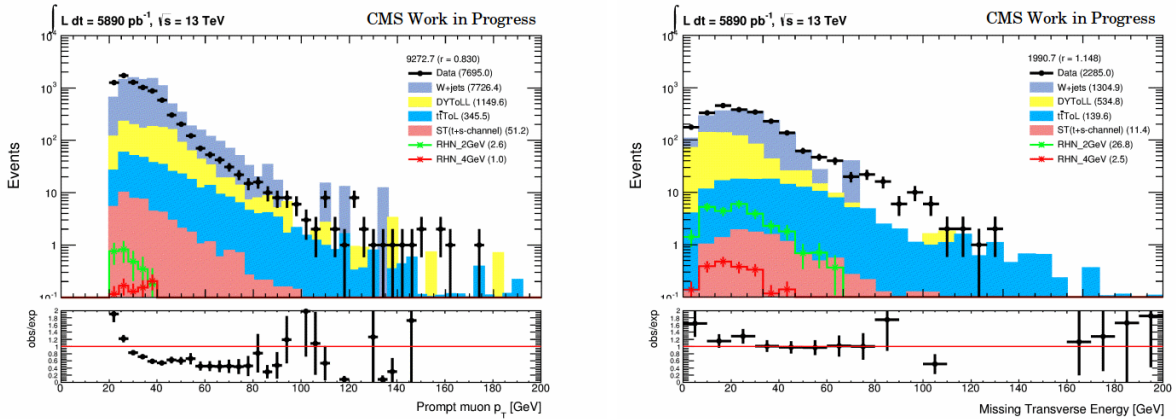


Figure 6.3: (a)  $p_T$  of the prompt muon with  $M(\mu_1, \mu_2, \mu_P) < 40$  GeV (left) and the missing transverse energy when  $M(\mu_1, \mu_2, \mu_P) > 80$  GeV (right)

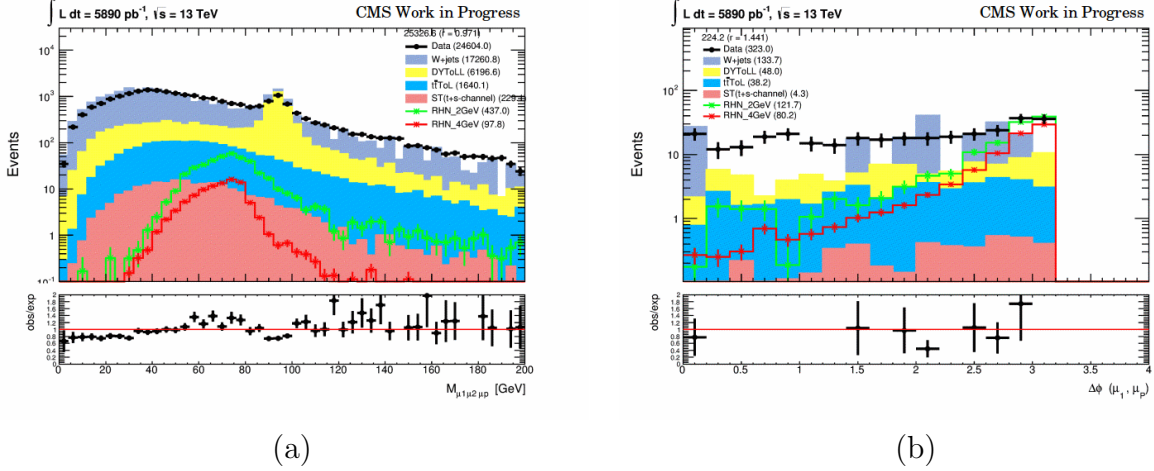


Figure 6.4: The  $M(\mu_1, \mu_2, \mu_P)$  (a), and the  $\Delta\phi$  between the prompt muon and the leading muon from the MuonJet (b). The invariant mass distribution shows contributions due to asymmetric conversions at the  $Z$ -mass.

one of the muon is lost and is not reconstructed and we are left with three muons which reconstruct to give the  $Z$  mass. About 80% of the background in the  $Z$  region is contributed by DY due to asymmetric conversion, as shown in Fig. 6.4 (a). Cosmic muons can also be a background, as they could emulate a pair of displaced muons, which lie back-to-back with each other. As shown in Fig 6.4 (a) the estimated MC backgrounds can explain the data within their statistical uncertainties. Hence, this background is expected to be not very significant. This is because in our case only  $\mu_1$  and  $\mu_2$  are displaced but lie very close to each other and hence cannot be emulated by the cosmics. Also, a very small fraction of the cosmics could fake the prompt muon, as they would have to pass through the exact collision point to do that. Nonetheless, a veto on cosmic background is applied as we take  $\Delta\phi < (\pi - 0.2)$  between  $\mu_1, \mu_P$ , and  $\mu_2, \mu_P$ .

Figure 6.5 shows the stacked plots of the background for the final set of selections. These have been overlaid with data and the signal points BP1 and BP2. The application of the condition of the opposite sign of  $\mu_1$  and  $\mu_2$  and  $d_{XY}$  of  $\mu_1$  and  $\mu_2$  improves the signal to background ratio after all the selection substantially. Table 6.1 shows the predicted number of events after final selection from SM backgrounds and for the two benchmark points. The observed data is also shown.

The  $W$ +jets sample is of very low luminosity and hence there is a very large scaling factor

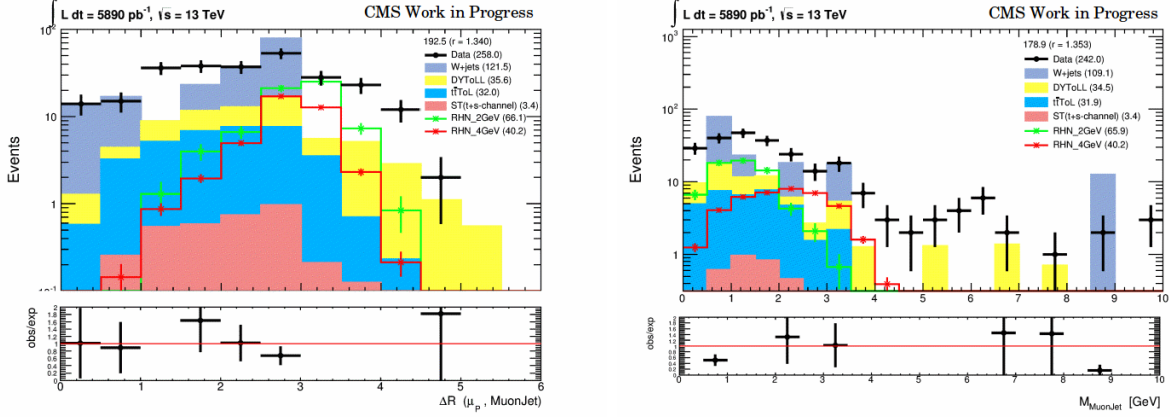


Figure 6.5: The  $\Delta R$  between the prompt muon and the MuonJet (left) and the invariant mass of the MuonJet shown between 0 and 10 GeV (right).

Samples	Number of Events (Pre-Selection)	Number of Events (Selection)
BP1	$391.7 \pm 8.2$	$66.4 \pm 3.4$
BP2	$9.5 \pm 0.1$	$4.04 \pm 0.09$
$W$ +jets	$20662.8 \pm 551.7$	$109.9 \pm 34.7$
$DY(\rightarrow ll)$ +jets	$4557.9 \pm 63.3$	$32.9 \pm 4.4$
$t\bar{t}(\rightarrow \nu lbb + jets)$	$1508.9 \pm 12.6$	$29.9 \pm 1.8$
Single Top	$209.2 \pm 3.1$	$3.4 \pm 0.4$
Data	$27232.6 \pm 184.3$	$236.0 \pm 14.6$

Table 6.1: Number of events passing the pre-selection and selection for signal, background and data for  $5.89 \text{ fb}^{-1}$  of data

and a very high statistical uncertainty ( $\sim 32\%$ ). Even though a more rigorous study and higher statistics in the  $W$ +jets sample could perhaps improve the data-background agreement in signal free region, the estimation is sufficient within the statistical uncertainties, for the sensitivity studies. For the sensitivity study, an additional veto on events with more than one prompt like muon was imposed, which cut down on the  $DY$  and  $W$ +jets background. Fig. 6.6 depicts the  $\Delta R$  between  $\mu_1$  and  $\mu_2$ , where the data is not unblinded and hence not shown in this plot.

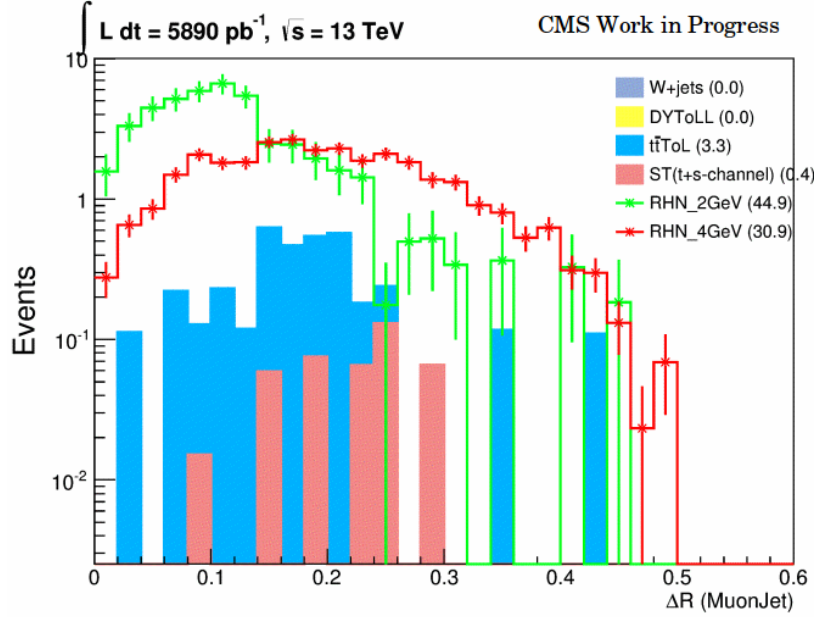


Figure 6.6:  $\Delta R$  between  $\mu_1$  and  $\mu_2$  from MuonJet after vetoing a second prompt

## 6.2 Sensitivity study at 13 TeV

We now proceed to estimate sensitivity for a 13 TeV collider. In this study, all the event selections were made on generator level objects, i.e. objects not passed through the detector simulation. Since this study was done using DELPHES, particle reconstruction efficiencies in DELPHES do not emulate the real detector perfectly for non-isolated and soft objects, such as the muons from MuonJets. Hence using reconstructed objects would not be as useful. To interpret the results in the terms of what we actually observe as data obtained at the LHC, different exclusion contours can be obtained by applying different reconstruction efficiencies to the truth objects.

### 6.2.1 Signal selections

To start with, the same set of selections used for the fully simulated signal point were used. They were imposed for selecting the generated level objects of DELPHES as well. The acceptance of the reconstructed objects of BP1 and BP2, was compared with the acceptance of the generated level objects of same two signal points, generated using DELPHES. It was

seen that the signal acceptance in fully reconstructed objects was greater than the signal acceptance for truth object ( 2.14 times more in BP1, and 1.16 times more in BP2 signal point ). A detailed study would be needed to understand the reason for this. Despite this, it wouldn't effect the results of this study. This is because the study is performed using generator level objects for both signal and background. Hence, the effect of reconstruction on event acceptance would be applicable to both. Since the senssitivity depends on the relative acceptance of signal and background, the sensitivity is expected to not change by much even for reconstructed objects.

The selections were modified to account for the generator level objects, the selections were slightly modified as variables such as impact parameter of an object depends on how it is reconstructed. Prompt muon selection criteria for the sensitivity studies was the same as it was for reconstructed objects in full simulation studies [Section 6.1.1] . For the selection of MuonJet, all possible pairs of muons with  $p_T > 2$  GeV,  $|\eta| < 2.4$  are considered. All the pre-selections described in Section 6.1.1 are applied. The muons from the MuonJet should always be opposite signed. The  $M(\mu_1, \mu_2, \mu_p) < 80$  GeV since we are probing the sub-weak model. The  $|d_{XY}| > 1$  mm cut is no longer imposed, as the  $|d_{XY}|$  is a parameter which depends a lot on how the displaced muon is reconstructed. Also through this study, it was observed that only a particular phase space of the signal points are favoured after imposing the  $|d_{XY}|$  cut, as only the signal points with MuonJets which are substantially displaced pass through the selection criteria, without significantly changing background yield. Fig. 6.7 shows the acceptance of the signal for the selection criteria used in Section 6.1.1 and for the selection criteria used for this sensitivity study. All events with more than one muon satisfying the prompt condition are vetoed.

The vetoing of events with more than one prompt cuts down on all the DY background and brings down the  $W$ +jets background. Hence  $t\bar{t}$ -semiLep is left as the dominant background and  $Wcc$  gives a small contribution in the signal region. Table 6.2 shows the signal and background events after the selections.

## 6.2.2 Result

For the sensitivity study both the MC background and the signal were scaled to  $30 \text{ fb}^{-1}$ , which is comparable to the data collected at the LHC in 2016, as well as  $300 \text{ fb}^{-1}$  of

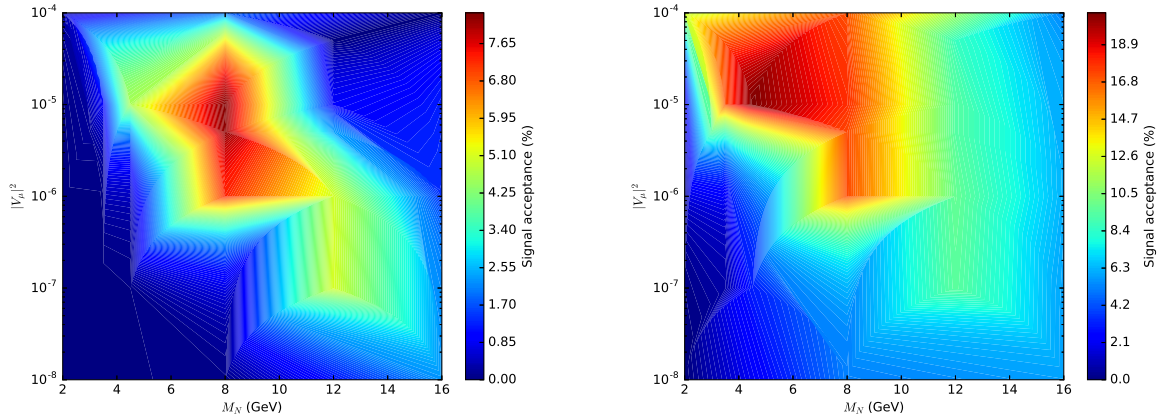


Figure 6.7: Acceptance for signal selections described in Section 6.1 (left) and acceptance for selections described in Section 6.2 (right) for a 13 TeV collider

Samples	Number of Events (Selection)
BP1	$10577.7 \pm 303.5$
BP2	$174.8 \pm 3.3$
$Wcc$	$73.7 \pm 12.7$
$t\bar{t}(\rightarrow \nu lbb + jets)$	$11082.6 \pm 342.3$

Table 6.2: Number of events passing selection for the sensitivity study, in signal points BP1 and BP2 and background, of luminosity  $30 \text{ fb}^{-1}$ .

luminosity. The expected limits for the sub-weak RHN model were calculated using the Higgs Combine tool, using the asymptotic limit method [68]-[71]. Shown below is the expected exclusion contour for three different detector efficiencies applied to the gen-level objects of DELPHES, at 100%, 70% and 50% efficiency. The expected exclusion contours are imposing the new selections used for gen-level objects of DELPHES, as shown in Fig. 6.8. It can be seen clearly that the selections used for the fully reconstructed objects do better as compared to the selections used for gen-level objects for the signal phase space which gives displaced MuonJets, while doing worse for signal phase space which give MuonJet with low displacement.

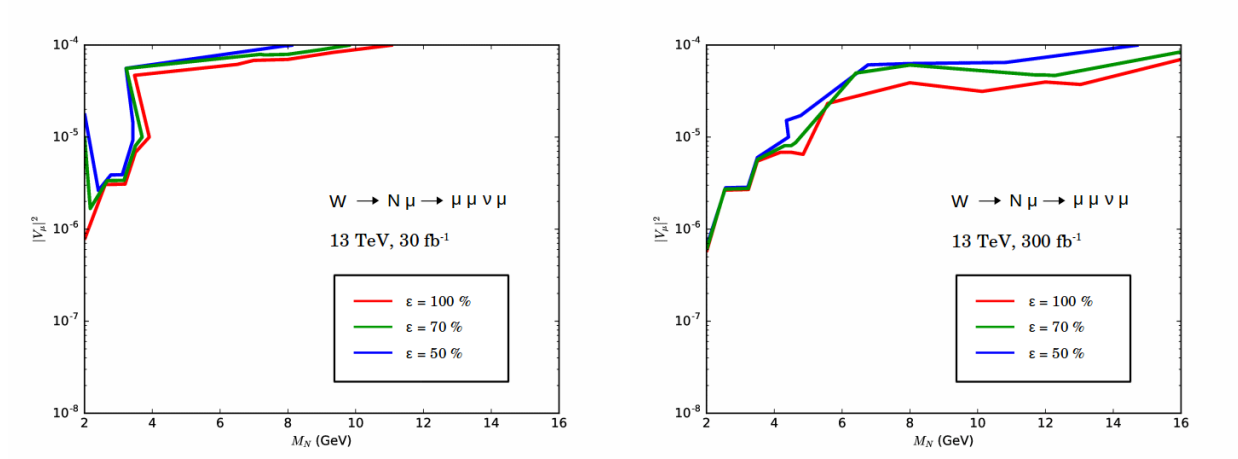


Figure 6.8: Exclusion contour at 13 TeV for integrated luminosity of 30 fb<sup>-1</sup> (left) and 300 fb<sup>-1</sup> (right). Each figure shows the contours for signal efficiency of 100%, 70%, and 50%. In each case, the selection is assumed to be 100% efficient for SM background.





# Chapter 7

## RHN studies at a 100 TeV hadron collider

With almost an order of magnitude increase in the centre-of-mass energy of proton collisions as compared to the LHC, the reach of a 100 TeV collider to explore new physics is expected to improve. It becomes important to study how it fares as compared to the LHC, for various different physics scenarios. This chapter gives an estimation of how sensitive a 100 TeV collider is to the RHN model for the phase space of  $M_N < 15$  GeV .

The sensitivity study of the RHN at 100 TeV was preceded by comparing how the signal at a 100 TeV collider behaves from the signal at 13 TeV collider, shown in Fig. 7.1. Signal of mass 8 GeV ,  $|V_\mu|^2 = 10^{-5}$  was generated in  $\sqrt{s}=13$  TeV as well as  $\sqrt{s}=100$  TeV COM energy, and the samples from the two different colliders were compared against each other. For the 8 GeV signal point the total momentum,  $P$ , of the generated level objects increases, but not by a substantial amount. Also for the 8 GeV point, the transverse momentum  $p_T$  of objects also increase, though again this increase is not much. On the other hand  $|\eta|$  distribution of the objects shifts towards higher values in a 100 TeV collider as compared to 13 TeV collider. This can be expected due to production increases in forward direction. Due to the observation that the  $p_T$  distribution of objects in a 100 TeV collider do not differ much as compared to a 13 TeV collider, we already get the idea that tightening the  $p_T$  cut might not increase the signal acceptance. The  $|\eta|$  cut however can be made looser, as keeping the same  $|\eta|$  cut as that of 13 TeV might reduce the signal acceptance, though these studies will

be discussed in detail, in the following section.

## 7.1 Signal selection

For the 100 TeV sensitivity study, as mentioned before, tightening the  $p_T$  cut was not beneficial for the signal acceptance as  $p_T$  does not differ by much in a 100 TeV collider. Additionally, keeping the  $|\eta| < 2.4$  condition was reducing the signal acceptance in the 100 TeV collider as compared to the 13 TeV collider, since the distribution of  $|\eta|$  for all the muons in the final signal topology had a much wider distribution.

For prompt selection, the cut  $|\eta| < 5$  was imposed, while all the other selection criteria are the same as the criteria used for selecting a prompt in a 13 TeV collider, as given in Section 6.2. For the selection of MuonJet, all possible pairs of muons with  $p_T > 2$  GeV,  $|\eta| < 5$  are now considered as candidates. The current colliders at the LHC do not have muon chambers with high  $|\eta|$  value coverage. Nonetheless it is reasonable to impose the  $|\eta| < 5$  cut, as the detector for a 100 TeV collider can be expected to have muon chambers even at such high  $|\eta|$  values, due to increase in particles in the forward direction. This implies that the forward detectors of the 100 TeV detector would have to be very efficient in reconstructing muon. The rest of the selections are the same as that of the 13 TeV collider. [ Section 6.2 ]

The same backgrounds contributing in the 13 TeV collider selections will contribute in the 100 TeV collider as well. Hence,  $t\bar{t}$ -semilep is the dominant background, followed by Wcc. As shown in table 3.3, the  $t\bar{t}$ -semilep background cross-section goes up by a factor of 50 in the 100 TeV collider as compared to the 13 TeV one. Hence, to reduce the  $t\bar{t}$ -semiLep background b-jet veto has been applied for 100 TeV selections, where b tagging efficiency is considered to be 0.7, which cuts down 91% of  $t\bar{t}$ -semiLep, since there are two b-jets and tagging even one of them rejects the background. Section 3.1.2 , lists down all the signal samples generated and Section 3.2.2 lists down the background generated for this study. Table 7.1 shows the signal and background events after applying the selections.

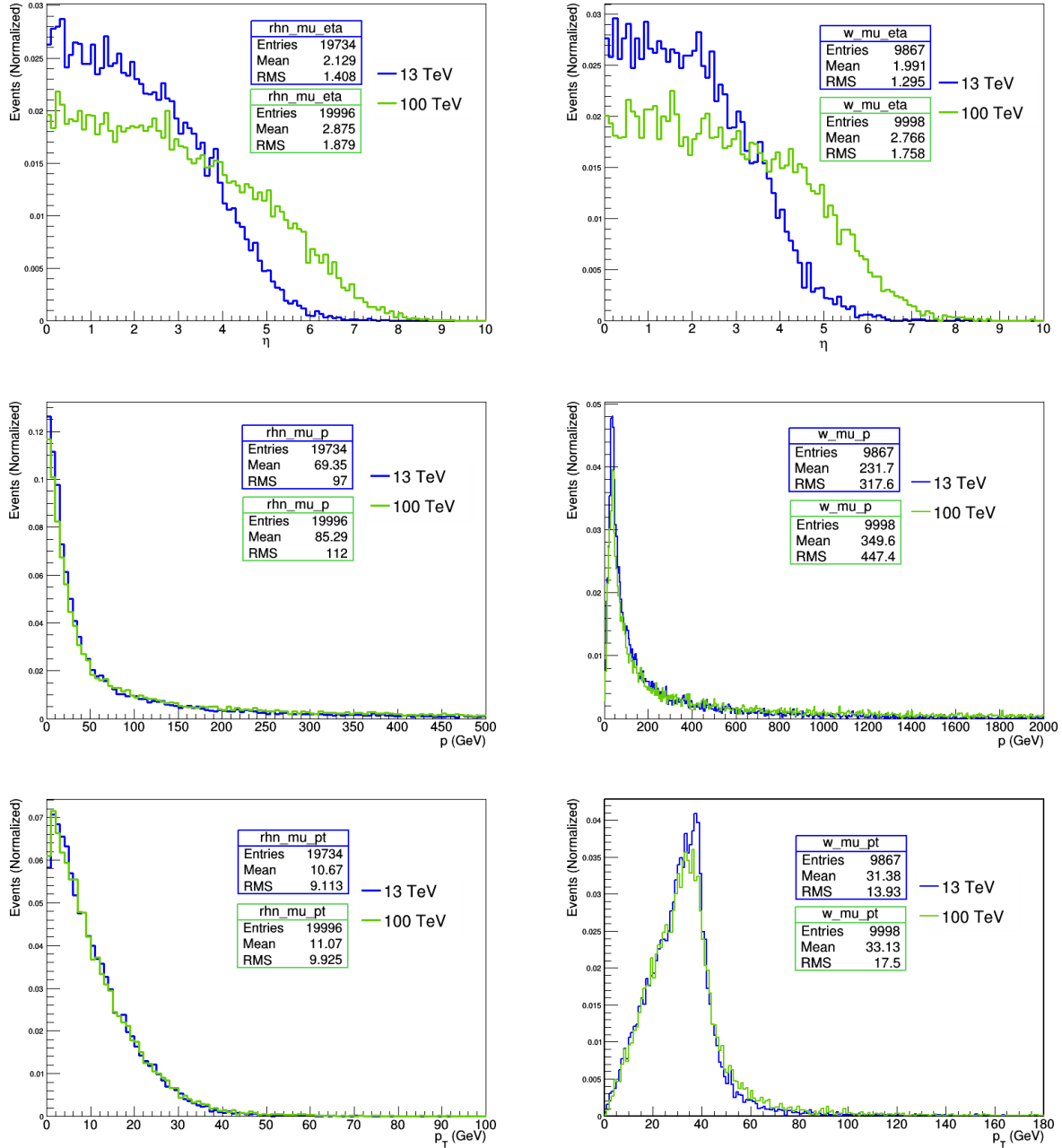


Figure 7.1: Various kinematic properties for the final state are compared at 13 TeV, and 100 TeV. The  $\eta$  of MuonJet muons (top, left), the eta of the prompt muon (top, right), the momentum ( $|\vec{p}|$ ) of MuonJet muons (middle, left), the  $|\vec{p}|$  of the prompt muon (middle, right), the  $p_T$  of MuonJet muons (bottom, left), and the  $p_T$  of the prompt muon (bottom, right). Aside from the  $\eta$ , all other distributions do not show large difference.

Samples	Number of Events (Selection)
BP1	$1222802.7 \pm 40873.8$
BP2	$10724.4 \pm 294.3$
$W_{cc}$	$10314.9 \pm 2431.2$
$t\bar{t}(\rightarrow \nu lbb + jets)$	$468104.8 \pm 9312.2$

Table 7.1: Number of events passing selection for the sensitivity study, in signal points BP1 and BP2 and background, of luminosity  $300 \text{ fb}^{-1}$ .

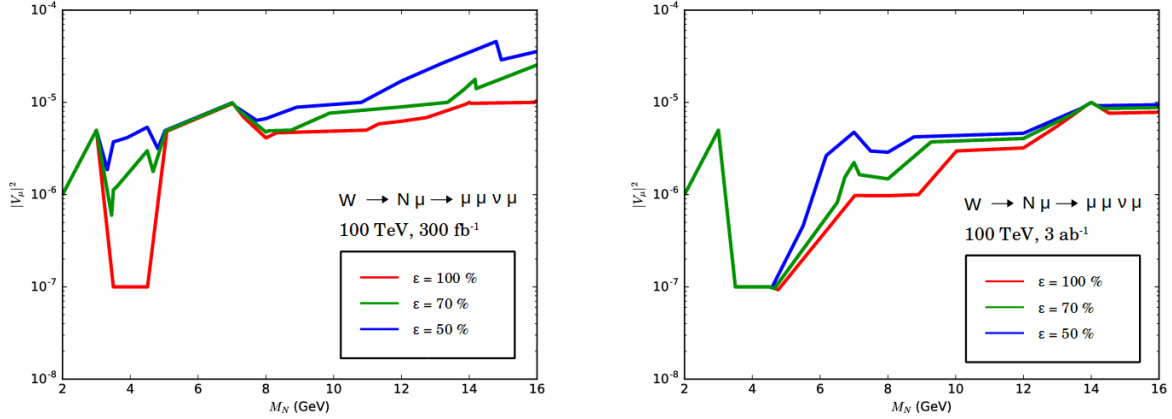


Figure 7.2: Exclusion contour at 100 TeV for integrated luminosity of  $300 \text{ fb}^{-1}$  (left) and  $3 \text{ ab}^{-1}$  (right). Each figure shows the contours for signal efficiency of 100%, 70%, and 50%. In each case, the selection is assumed to be 100% efficient for SM background.

## 7.2 Result

For the sensitivity study both the MC background and the signal were scaled to  $300 \text{ fb}^{-1}$ , which is comparable to the data expected to be collected at the LHC, as well as  $3 \text{ ab}^{-1}$  of luminosity. The expected limits for the sub-weak RHN model were calculated using the Higgs Combine tool, using the asymptotic limit method. Shown in Fig. 7.2 is the expected exclusion contour for three different detector efficiencies applied to the gen-level objects of DELPHES, at 100%, 70% and 50% efficiency.

# Chapter 8

## Conclusion

Sensitivity study for the RHN model, for the phase space of  $M_N < 16$  GeV was carried out in a 13 TeV collider as well 100 TeV collider. The background estimation was cross-checked using 16% of the 2016 data and was found to be a comprehensive within 20% of the data, in a signal free-region. It was observed that the acceptance of signal and background for the 100 TeV collider had increased as compared to the 13 TeV collider as shown in Table 8.1 due to the change in  $|\eta|$  cut.

The sensitivity of the FCC-hh as compared to the LHC also depends on how the cross-section of the background and signal differ in both. As already shown in the Section 3.1.2 and Section 3.2.2, the cross-section of signal goes up by a maximum of a factor of 12, while the background cross-section goes up by a factor of 50. Since the signal involves only the weak processes and leptonic decay modes, unlike the background where  $t\bar{t}$ -semiLep involves strong interactions, the cross-sectional change in signal is much lesser than that of the background. Therefore, the background contributes much more in the 100 TeV collider as compared to the 13 TeV . To reduce the  $t\bar{t}$ -semiLep background at the 100 TeV collider, it is b-tagged with an efficiency of 91% and the b-tagged events are vetoed. Thus, the change in  $|\eta|$  cut along with b-tag veto on  $t\bar{t}$ -semiLep background increases the reach of the 100 TeV collider as compared to the 13 TeV one. Fig. 8.1 compares the exclusion contour for  $300 \text{ fb}^{-1}$  of data in 13 TeV and 100 TeV, for a reconstruction efficiency of 100%. The 100 TeV collider is expected to collect  $3 \text{ ab}^{-1}$  luminosity of data. With the given luminosity of  $3 \text{ ab}^{-1}$  , the sensitivity of the 100 TeV collider surpasses the sensitivity of the 13 TeV collider for 300

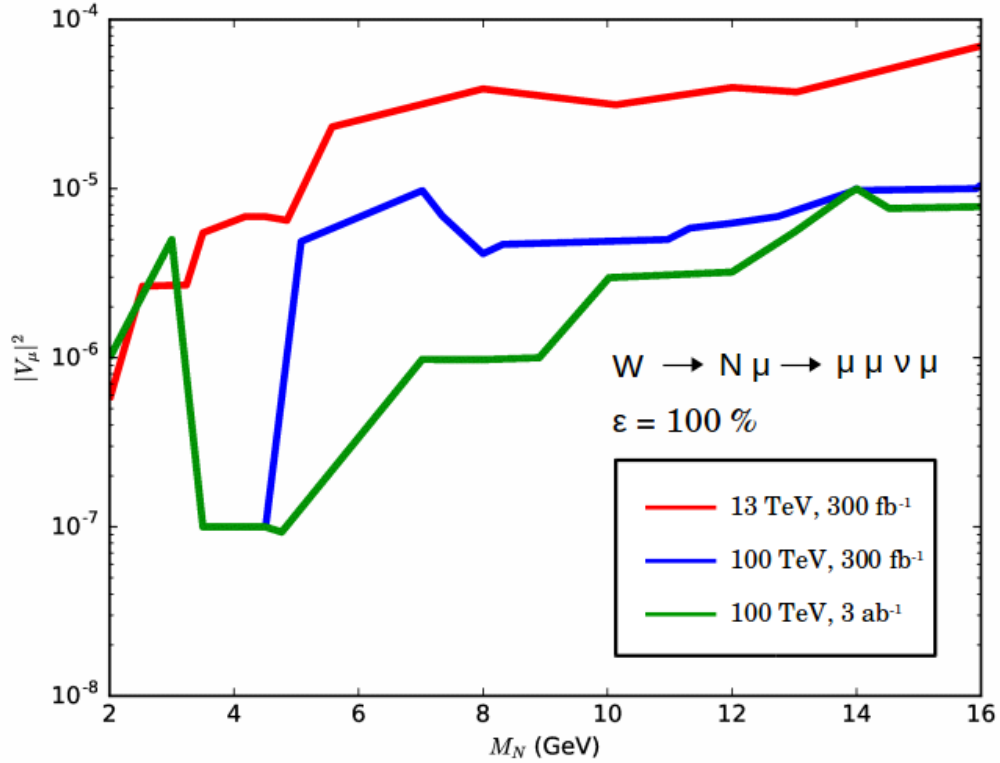


Figure 8.1: Exclusion contours at  $\sqrt{s} = 13$  TeV and 100 TeV for signal efficiency of 100%. For the same luminosity of  $300 \text{ fb}^{-1}$ , the 100 TeV collider has a higher reach than the 13 TeV one. This is due to increase in signal acceptance and cross-section at the 100 TeV collider. The reach of the 100 TeV collider further increases, corresponding to a luminosity of  $3 \text{ ab}^{-1}$  of data.

Signal Mass (GeV)	Signal Mixing ( $ V_\mu ^2$ )	Sig. Acc. :13 TeV(%)	Sig. Acc. :100 TeV(%)
2	$10^{-4}$	0.121	0.214
2	$10^{-6}$	0.003	0.004
2	$10^{-8}$	0.00	0.00
4	$10^{-4}$	0.257	0.499
4	$5 \times 10^{-5}$	0.247	0.491
4	$10^{-5}$	0.264	0.306
4	$5 \times 10^{-6}$	0.257	0.161
4	$10^{-7}$	0.019	0.030
8	$10^{-4}$	0.169	0.271
8	$10^{-5}$	0.179	0.272
8	$5 \times 10^{-6}$	0.173	0.273
8	$10^{-6}$	0.172	0.270
8	$10^{-7}$	0.109	0.180
8	$10^{-8}$	0.052	0.076
12	$5 \times 10^{-5}$	0.086	0.147
12	$10^{-5}$	0.094	0.159
12	$5 \times 10^{-6}$	0.094	0.161
12	$10^{-6}$	0.098	0.162
12	$10^{-7}$	0.095	0.178
16	$10^{-4}$	0.053	0.091
16	$10^{-6}$	0.062	0.091
16	$10^{-8}$	0.058	0.098

Table 8.1: Signal acceptance for 13 TeV and 100 TeV

$\text{fb}^{-1}$  of data, as shown in Fig. 8.1.





# Chapter 9

## Appendix

Background	Production Details
$W(\rightarrow \nu l)+jets$	TuneCUETP8M1_13TeV-madgraphMLM-pythia8 RunIISpring16MiniAODv2-PUSpring16_80X
$DY(\rightarrow ll)+jets$ (M10to50)	TuneCUETP8M1_13TeV-madgraphMLM-pythia8 RunIISpring16MiniAODv2-PUSpring16_80X
$DY(\rightarrow ll)+jets$ (M-50)	TuneCUETP8M1_13TeV-madgraphMLM-pythia8 RunIISpring16MiniAODv2-PUSpring16_80X
$t\bar{t}(\rightarrow \nu lbb + jets)$	TuneCUETP8M1_13TeV-madgraphMLM-pythia8 RunIISpring16MiniAODv2-PUSpring16_80X
<i>Single Top t – channel + jets</i>	13TeV-powheg-pythia8_TuneCUETP8M1 RunIISpring16MiniAODv2-PUSpring16_80X
<i>Single Top s – channel + jets</i>	13TeV-amcatnlo-pythia8_TuneCUETP8M1 RunIISpring16MiniAODv2-PUSpring16_80X

Table 9.1: Details about background samples generated using CMS FullSim at 13 TeV

Signal Mass (GeV)	Signal Mixing ( $ V_{\mu} ^2$ )	$\sigma(pb)$ (13 TeV)	$\sigma(pb)$ (100 TeV)
2	$10^{-4}$	2.90195	22.771
2	$10^{-6}$	2.91635	22.893
2	$5 \times 10^{-7}$	—	22.82
2	$10^{-7}$	—	21.67
2	$10^{-8}$	0.94859	7.867
4	$10^{-4}$	0.12775	0.4515
4	$5 \times 10^{-5}$	0.0735	0.2603
4	$10^{-5}$	0.02205	0.2692
4	$5 \times 10^{-6}$	0.03166	0.2457
4	$10^{-6}$	0.02964	0.2341
4	$10^{-7}$	0.03006	0.2331
4	$10^{-8}$	—	0.234
6	$10^{-6}$	—	0.0089
6	$5 \times 10^{-7}$	—	0.0078
8	$10^{-4}$	0.08289	0.6491
8	$10^{-5}$	0.00869	0.0659
8	$5 \times 10^{-6}$	0.00444	0.0341
8	$10^{-6}$	0.00109	0.0085
8	$5 \times 10^{-7}$	—	0.0023
8	$10^{-7}$	0.00035	0.0027
8	$10^{-8}$	0.00032	0.0025
10	$10^{-6}$	—	0.0068
12	$5 \times 10^{-5}$	0.03909	0.3019
12	$10^{-5}$	0.00782	0.0605
12	$5 \times 10^{-6}$	0.00391	0.0302
12	$10^{-6}$	0.000789	0.0061
12	$10^{-7}$	0.00009	0.0008
14	$10^{-5}$	—	0.0588
16	$10^{-4}$	0.07303	0.5732
16	$5 \times 10^{-5}$	—	0.2863
16	$10^{-5}$	—	0.0574
16	$10^{-6}$	0.000738	0.0057
16	$10^{-8}$	—	0.00008

Table 9.2: Signal cross-sections for 13 TeV and 100 TeV using DELPHES

# Bibliography

- [1] S. Chatrchyan *et al.* [CMS Collaboration], Phys. Lett. B **716** (2012) 30 doi:10.1016/j.physletb.2012.08.021 [arXiv:1207.7235 [hep-ex]].
- [2] G. Aad *et al.* [ATLAS Collaboration], Phys. Lett. B **716** (2012) 1 doi:10.1016/j.physletb.2012.08.020 [arXiv:1207.7214 [hep-ex]].
- [3] K. A. Olive *et al.* [Particle Data Group], Chin. Phys. C **38** (2014) 090001. doi:10.1088/1674-1137/38/9/090001
- [4] P. W. Higgs, Phys. Rev. Lett. **13** (1964) 508. doi:10.1103/PhysRevLett.13.508
- [5] F. Englert and R. Brout, Phys. Rev. Lett. **13** (1964) 321. doi:10.1103/PhysRevLett.13.321
- [6] Marino Missiroli and Jorge Fernandez de Trocniz. *Searches for top-antitop quark resonances in semileptonic final states with the CMS detector*. PhD thesis, Universidad Autnoma de Madrid, 2017. Presented 10 Mar 2017.
- [7] Javier Mauricio Duarte and Maria Spiropulu. *Naturalness confronts nature: searches for supersymmetry with the CMS detector in pp collisions at  $\sqrt{s} = 8$  and 13 TeV*. PhD thesis, Caltech, 2017. Presented 11 Aug 2016.
- [8] Johannes Lange and Lutz Werner Feld. *Search for electroweak production of supersymmetric particles with photonic final states using the first LHC Run II data recorded with the CMS detector*. PhD thesis, Hamburg U., 2016.
- [9] T.~S. van Albada, J.~N. Bahcall, K Begeman, and R Sancisi. Distribution of dark matter in the spiral galaxy NGC 3198. *\apj*, 295:305–313, aug 1985.
- [10] K. Garrett and G. Duda, Adv. Astron. **2011** (2011) 968283 doi:10.1155/2011/968283 [arXiv:1006.2483 [hep-ph]].
- [11] C. S. Wu, E. Ambler, R. W. Hayward, D. D. Hoppes and R. P. Hudson, Phys. Rev. **105**, 1413 (1957). doi:10.1103/PhysRev.105.1413

- [12] Raymond Davis, Don S. Harmer, and Kenneth C. Hoffman. Search for neutrinos from the sun. *Phys. Rev. Lett.*, 20:1205–1209, May 1968.
- [13] K. Lande *et al.*, AIP Conf. Proc. **243** (1992) 1122. doi:10.1063/1.41548
- [14] "The Nobel Prize in Physics 2015". Nobelprize.org. Nobel Media AB 2014. Web. 19 Mar 2017. [https://www.nobelprize.org/nobel\\_prizes/physics/laureates/2015/advanced-physicprize2015.pdf](https://www.nobelprize.org/nobel_prizes/physics/laureates/2015/advanced-physicprize2015.pdf)
- [15] Q. R. Ahmad, R. C. Allen, T. C. Andersen, et al. Measurement of day and night neutrino energy spectra at sno and constraints on neutrino mixing parameters. *Phys. Rev. Lett.*, 89:011302, Jun 2002.
- [16] Y. Fukuda *et al.* [Super-Kamiokande Collaboration], *Phys. Rev. Lett.* **81** (1998) 1562 doi:10.1103/PhysRevLett.81.1562 [hep-ex/9807003].
- [17] B. Pontecorvo, *Sov. Phys. JETP* 6, 429 (1957)
- [18] B. Pontecorvo, *Sov. Phys. JETP* 7,172 (1958)
- [19] Z. Maki, M. Nakagawa and S. Sakata, *Prog. in Theor. Phys.* 28, 870 (1962)
- [20] B. Pontecorvo, *Sov. Phys. JETP* 26, 984 (1968)
- [21] V.N. Gribov and B. Pontecorvo, *Phys. Lett. B*28, 493 (1969)
- [22] F. Boehm and P. Vogel. *Physics of Massive Neutrinos*. Cambridge University Press, 1992.
- [23] Takehiko Asaka, Steve Blanchet, and Mikhail Shaposhnikov. The  $\nu$ MSM, dark matter and neutrino masses. *Physics Letters B*, 631(4):151–156, 2005.
- [24] T. Asaka and M. Shaposhnikov, *Phys. Lett. B* **620** (2005) 17 doi:10.1016/j.physletb.2005.06.020 [hep-ph/0505013].
- [25] L. Canetti, M. Drewes, T. Frossard and M. Shaposhnikov, *Phys. Rev. D* **87** (2013) 093006 doi:10.1103/PhysRevD.87.093006 [arXiv:1208.4607 [hep-ph]].
- [26] P. Minkowski, *Phys. Lett. B* **67**, 421 (1977); M. Gell-Mann, P. Ramond and R. Slansky, *Supergravity*, North Holland, Amsterdam, 315 (1980); T. Yanagida, in *Proceedings of the Workshop on the Unified Theory and the Baryon Number in the Universe*, KEK, Tsukuba, Japan, 95 (1979); S. L. Glashow, in *Proceedings of the 1979 Cargese Summer Institute on Quarks and Leptons*, Plenum Press, New York, 687 (1980); R. N. Mohapatra and G. Senjanovic, *Phys. Rev. Lett.* **44**, 912 (1980); J. Schechter and J. W. F. Valle, *Phys. Rev. D* **22**, 2227 (1980); J. Schechter and J. W. F. Valle, *Phys. Rev. D* **25**, 774 (1982).

- [27] F. F. Deppisch, P. S. Bhupal Dev and A. Pilaftsis, *New J. Phys.* **17** (2015) no.7, 075019 doi:10.1088/1367-2630/17/7/075019 [arXiv:1502.06541 [hep-ph]].
- [28] M.E. Peskin and D.V. Schroeder. *An Introduction to Quantum Field Theory*. Advanced book classics. Avalon Publishing, 1995.
- [29] R. D. Klauber, "The Seesaw Mechanism"  
<http://www.quantumfieldtheory.info/TheSeesawMechanism.pdf>
- [30] S. T. Petcov, *Adv. High Energy Phys.* **2013** (2013) 852987 doi:10.1155/2013/852987 [arXiv:1303.5819 [hep-ph]].
- [31] E. Izaguirre and B. Shuve, *Phys. Rev. D* **91** (2015) no.9, 093010 doi:10.1103/PhysRevD.91.093010 [arXiv:1504.02470 [hep-ph]].
- [32] D. Gorbunov and I. Timiryasov, *Phys. Lett. B* **745** (2015) 29 doi:10.1016/j.physletb.2015.02.060 [arXiv:1412.7751 [hep-ph]].
- [33] T. Yamazaki *et al.*, *Conf. Proc. C* **840719** (1984) 262.
- [34] G. Bernardi *et al.*, *Phys. Lett.* **166B** (1986) 479. doi:10.1016/0370-2693(86)91602-3
- [35] H. Grassler *et al.* (BEBC WA66), *Nucl.Phys. B*273, 253 (1986).
- [36] O Adriani *et al.* Search for isosinglet neutral heavy leptons in Z0 decays. *Physics Letters B*, 295(3):371–382, 1992.
- [37] P. Astier *et al.* [NOMAD Collaboration], *Phys. Lett. B* **506** (2001) 27 doi:10.1016/S0370-2693(01)00362-8 [hep-ex/0101041].
- [38] P. Abreu *et al.* [DELPHI Collaboration], *Z. Phys. C* **74** (1997) 57 Erratum: [*Z. Phys. C* **75** (1997) 580]. doi:10.1007/s002880050370
- [39] A. Vaitaitis *et al.* [NuTeV and E815 Collaborations], *Phys. Rev. Lett.* **83** (1999) 4943 doi:10.1103/PhysRevLett.83.4943 [hep-ex/9908011].
- [40] A. Boyarsky, O. Ruchayskiy and M. Shaposhnikov, *Ann. Rev. Nucl. Part. Sci.* **59** (2009) 191 doi:10.1146/annurev.nucl.010909.083654 [arXiv:0901.0011 [hep-ph]].
- [41] O. Ruchayskiy and A. Ivashko, *JCAP* **1210** (2012) 014 doi:10.1088/1475-7516/2012/10/014 [arXiv:1202.2841 [hep-ph]].
- [42] Search for Majorana neutrino production in pp collisions at  $\sqrt{s}=7$  TeV in dimuon final states with the ATLAS detector. Technical Report ATLAS-CONF-2012-139, CERN, Geneva, Sep 2012.
- [43] D. Liventsev *et al.* [Belle Collaboration], *Phys. Rev. D* **87** (2013) no.7, 071102 doi:10.1103/PhysRevD.87.071102 [arXiv:1301.1105 [hep-ex]].

- [44] A. V. Artamonov *et al.* [E949 Collaboration], Phys. Rev. D **91** (2015) no.5, 052001 Erratum: [Phys. Rev. D **91** (2015) no.5, 059903] doi:10.1103/PhysRevD.91.059903, 10.1103/PhysRevD.91.052001 [arXiv:1411.3963 [hep-ex]].
- [45] V. Khachatryan *et al.* [CMS Collaboration], Phys. Lett. B **748** (2015) 144 doi:10.1016/j.physletb.2015.06.070 [arXiv:1501.05566 [hep-ex]].
- [46] A. M. Sirunyan *et al.* [CMS Collaboration], arXiv:1703.03995 [hep-ex].
- [47] V. Khachatryan *et al.* [CMS Collaboration], JHEP **1604** (2016) 169 doi:10.1007/JHEP04(2016)169 [arXiv:1603.02248 [hep-ex]].
- [48] G. Aad *et al.* [ATLAS Collaboration], JHEP **1507** (2015) 162 doi:10.1007/JHEP07(2015)162 [arXiv:1506.06020 [hep-ex]].
- [49] G. Aad *et al.* [ATLAS Collaboration], Eur. Phys. J. C **72** (2012) 2056 doi:10.1140/epjc/s10052-012-2056-4 [arXiv:1203.5420 [hep-ex]].
- [50] D. Curtin, R. Essig, S. Gori and J. Shelton, JHEP **1502** (2015) 157 doi:10.1007/JHEP02(2015)157 [arXiv:1412.0018 [hep-ph]].
- [51] C. Cheung, J. T. Ruderman, L. T. Wang and I. Yavin, JHEP **1004** (2010) 116 doi:10.1007/JHEP04(2010)116 [arXiv:0909.0290 [hep-ph]].
- [52] S. Chatrchyan *et al.* [CMS Collaboration], JHEP **1107** (2011) 098 doi:10.1007/JHEP07(2011)098 [arXiv:1106.2375 [hep-ex]].
- [53] G. Aad *et al.* [ATLAS Collaboration], JHEP **1602** (2016) 062 doi:10.1007/JHEP02(2016)062 [arXiv:1511.05542 [hep-ex]].
- [54] M. Buschmann, J. Kopp, J. Liu and P. A. N. Machado, JHEP **07** (2015) 045 doi:10.1007/JHEP07(2015)045 [arXiv:1505.07459 [hep-ph]].
- [55] V. Khachatryan *et al.* [CMS Collaboration], Phys. Lett. B **752** (2016) 146 doi:10.1016/j.physletb.2015.10.067 [arXiv:1506.00424 [hep-ex]].
- [56] T. Sjostrand, S. Mrenna and P. Z. Skands, Comput. Phys. Commun. **178** (2008) 852 doi:10.1016/j.cpc.2008.01.036 [arXiv:0710.3820 [hep-ph]].
- [57] T. Sjostrand, S. Mrenna and P. Z. Skands, JHEP **0605** (2006) 026 doi:10.1088/1126-6708/2006/05/026 [hep-ph/0603175].
- [58] J. Alwall *et al.*, JHEP **1407**, 079 (2014) doi:10.1007/JHEP07(2014)079 [arXiv:1405.0301 [hep-ph]].
- [59] A. Alloul, N. D. Christensen, C. Degrande, C. Duhr and B. Fuks, Comput. Phys. Commun. **185** (2014) 2250 doi:10.1016/j.cpc.2014.04.012 [arXiv:1310.1921 [hep-ph]].

- [60] M. H. Seymour and M. Marx, doi:10.1007/978-3-319-05362-2\_8 arXiv:1304.6677 [hep-ph].
- [61] A. Buckley, J. Ferrando, S. Lloyd, K. Nordström, B. Page, M. Rfenacht, M. Schnherr and G. Watt, Eur. Phys. J. C **75** (2015) 132 doi:10.1140/epjc/s10052-015-3318-8 [arXiv:1412.7420 [hep-ph]].
- [62] Tejinder S Virdee. Experimental techniques. (CERN-OPEN-2000-261), 1999.
- [63] S Agostinelli, J Allison, K Amako, et al. Geant4a simulation toolkit. *Nuclear Instruments and Methods in Physics Research Section A: Accelerators, Spectrometers, Detectors and Associated Equipment*, 506(3):250–303, 2003.
- [64] J. Allison, K. Amako, J. Apostolakis, et al. Geant4 developments and applications. *IEEE Transactions on Nuclear Science*, 53(1):270–278, Feb 2006.
- [65] J. de Favereau *et al.* [DELPHES 3 Collaboration], JHEP **1402** (2014) 057 doi:10.1007/JHEP02(2014)057 [arXiv:1307.6346 [hep-ex]].
- [66] G L Bayatian, S Chatrchyan, G Hmayakyan, and Sirunyan, et al. *CMS Physics: Technical Design Report Volume 1: Detector Performance and Software*. Technical Design Report CMS. CERN, Geneva, 2006.
- [67] David Barney. CMS Detector Slice. CMS Collection., Jan 2016.
- [68] T. Junk, Nucl. Instrum. Meth. A **434** (1999) 435 doi:10.1016/S0168-9002(99)00498-2 [hep-ex/9902006].
- [69] A. L. Read, Modified frequentist analysis of search results (the CLs method) in Workshop on Confidence Limits, Eds. F. James, L. Lyons, and Y. Perrin., p. 81.
- [70] A L Read. Presentation of search results: the CL<sub>s</sub> technique. *J. Phys. G*, 28(10):2693–704, 2002.
- [71] Procedure for the LHC Higgs boson search combination in Summer 2011. Technical Report CMS-NOTE-2011-005. ATL-PHYS-PUB-2011-11, CERN, Geneva, Aug 2011.